

Accepted Manuscript

Multiphase magma intrusion, ore-enhancement and hydrothermal carbonatisation in the Siah-Kamar porphyry Mo deposit, Urumieh-Dokhtar magmatic zone, NW Iran

Ahmad Rabiee, Federico Rossetti, Francesca Tecce, Yoshihiro Asahara, Hossein Azizi, Johannes Glodny, Federico Lucci, Reza Nozaem, Joachim Opitz, David Selby

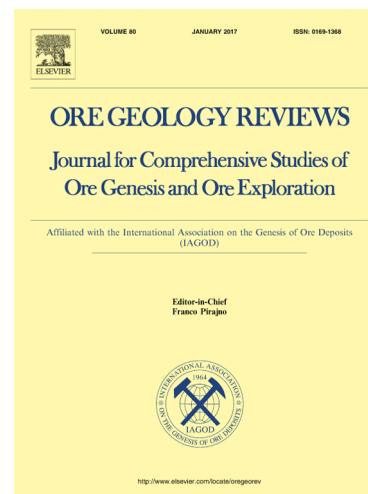
PII: S0169-1368(19)30160-X
DOI: <https://doi.org/10.1016/j.oregeorev.2019.05.016>
Reference: OREGEO 2930

To appear in: *Ore Geology Reviews*

Received Date: 22 February 2019
Revised Date: 8 May 2019
Accepted Date: 13 May 2019

Please cite this article as: A. Rabiee, F. Rossetti, F. Tecce, Y. Asahara, H. Azizi, J. Glodny, F. Lucci, R. Nozaem, J. Opitz, D. Selby, Multiphase magma intrusion, ore-enhancement and hydrothermal carbonatisation in the Siah-Kamar porphyry Mo deposit, Urumieh-Dokhtar magmatic zone, NW Iran, *Ore Geology Reviews* (2019), doi: <https://doi.org/10.1016/j.oregeorev.2019.05.016>

This is a PDF file of an unedited manuscript that has been accepted for publication. As a service to our customers we are providing this early version of the manuscript. The manuscript will undergo copyediting, typesetting, and review of the resulting proof before it is published in its final form. Please note that during the production process errors may be discovered which could affect the content, and all legal disclaimers that apply to the journal pertain.



1 **Multiphase magma intrusion, ore-enhancement and**
2 **hydrothermal carbonatisation in the Siah-Kamar porphyry Mo**
3 **deposit, Urumieh-Dokhtar magmatic zone, NW Iran**

4
5 Ahmad Rabiee¹, Federico Rossetti^{1,*}, Francesca Tecce², Yoshihiro Asahara³, Hossein Azizi⁴, Johannes
6 Glodny⁵, Federico Lucci¹, Reza Nozaem⁶, Joachim Opitz⁷, David Selby^{8,9}

7
8 ¹ *Dipartimento di Scienze, Università degli Studi Roma Tre, Roma, Italy*

9 ² *Istituto di Geologia Ambientale e Geoingegneria, CNR, Rome, Italy*

10 ³ *Department of Earth and Environmental Sciences, Nagoya University, Nagoya, Japan*

11 ⁴ *Mining Department, Faculty of Engineering, University of Kurdistan, Sanandaj, Iran.*

12 ⁵ *GFZ German Research Centre for Geosciences, Potsdam, Germany*

13 ⁶ *School of Geology, University of Tehran, Tehran, Iran*

14 ⁷ *Institut für Mineralogie und Kristallchemie, Universität Stuttgart, Stuttgart, Germany*

15 ⁸ *Department of Earth Sciences, Durham University, Durham, UK*

16 ⁹ *State Key Laboratory of Geological Processes and Mineral Resources, School of Earth Resources,*
17 *China University of Geosciences, Wuhan, China*

18

19

20

21

22

23

24

25 *Corresponding Author:

26 Dipartimento di Scienze

27 Sezione di Scienze Geologiche

28 Università Roma Tre

29 Largo S. L. Murialdo, 1

30 00146 Roma (ITALY)

31 Phone: +390657338043

32 FAX: +390657338201

33 e-mail: federico.rossetti@uniroma3.it

34 Skype: fede.rossetti

35
36
37
38
39
40
41
42
43
44
45
46
47
48
49
50
51
52
53
54
55
56
57
58
59
60
61
62
63
64
65
66
67
68

Abstract

The Siah-Kamar Mo deposit (SKMD) is located at the northwestern termination of the Urumieh-Dokhtar magmatic zone and it is the only porphyry Mo ore reserve in Iran. The exploration program documented 39.2 Mt proved reserves @ 539 ppm Mo and 66.4 Mt probable reserves @ 266 ppm Mo. In this study, field and petrographic investigations, integrated with geochemical (fluid inclusion and quartz chemistry) and geochronological (U-Pb zircon, Re-Os molybdenite, and Rb-Sr multiminerall isochron) studies are used to propose a metallogenic model for the Mo mineralisation in the SKMD. The geology of the SKMD is characterized by the emplacement of a multiphase Oligocene basic/intermediate (at ca. 33-30 Ma) to acidic (29-28 Ma) magmatic suite, which intruded the Eocene volcanic country rocks. The alteration zone, about 4×3 km in size and with a general NW-SE trend, is centered within the main basic porphyry stock, grading from an inner potassic-sodic zone to peripheral phyllic/propylitic halos. The late acidic magmatic products (stocks and dykes) intruded and post-dated the main alteration zone. Two-stage Mo mineralisation is recognised, including: (i) stage-1, disseminated molybdenite, coeval with the formation of potassic-sodic alteration and minor, microscale Fsp, Bt, Qz+Po veinlets; and (ii) stage-2, high-grade molybdenite+carbonate (\pm sericite), structurally-controlled stockwork veining. Fluid inclusion systematics combined with TitaniQ thermometry documents a mineralising fluid system compatible with a transition from high-temperature (up to ca. 600 °C) magmatic to epithermal (250 °C) conditions during progressive cooling, exhumation and mixing with meteoric sources at shallow crustal conditions (ca. 7-3 km). The Re-Os molybdenite dating constrains the high-grade Mo ore formation at ca. 29-28 Ma, attesting for the intimate linkage between the main Mo mineralisation and the acidic magmatic phase in the area. The Rb-Sr geochronology of the potassic-sodic alteration zones confirms the two-stage magmatic/mineralisation scenarios, overlapping within errors with the results obtained from the U-Pb zircon geochronology and constraining the formation of the potassic-sodic and phyllic alteration at ca. 33 and 28 Ma, respectively. Our results document an uncommon scenario of two-stage porphyry Mo mineralisation associated with intensive late stage carbonate precipitation and achieved during a long-lasting and multiphase magmatic pulses of Oligocene age. We highlight the dominant role of acidic fluid neutralisation for further ore enrichment during polyphase magma intrusion as the dominant factor controlling the Mo mineralisation in the SKMD. Comparison at a regional-scale indicates that parameters such as longevity of magma supply, progressive magma crystallization/differentiation, and the

69 presence of a possible pre-enriched crustal material should be considered responsible for the
70 Mo endowment in the UDMZ.

71

72 **Key words:** porphyry Mo, ore deposits, magmatism, fluids, Urumieh-Dokhtar zone, Iran

73

74 **1. Introduction**

75 Molybdenum (Mo) porphyry-type deposits supply the main Mo demands worldwide (>
76 95%) (John and Taylor, 2016). The Mo deposits are mainly associated with subduction-
77 related settings, such as volcano-plutonic magmatic arcs, back-arcs and continental collision
78 orogens (Westra and Keith, 1981; Wallace, 1995; Seedorff et al., 2005; Taylor et al., 2012;
79 Wu et al., 2017). They are mainly located in the western Cordillera of North America (Ayres
80 et al., 1982; Duke, 2007; Kerr et al., 2009), in Eastern Europe (Janković, 1982), Australia
81 (Whitcher, 1975), China (Mao et al., 2008; Zeng et al., 2012; Wu et al., 2017), Russia
82 (Sutulov, 1973), and elsewhere in Asia (Heinhorst et al., 2000).

83 Porphyry molybdenum deposits have been classified based on the Mo modal abundance, F
84 content, geochemical fingerprint of associated magmatism, and geodynamic setting of
85 formation (Westra and Keith, 1981; Ludington et al., 2009; Ludington and Plumlee, 2009;
86 Taylor et al., 2012; Wu et al., 2017). In particular, two end-member porphyry Mo
87 mineralisation types have been proposed in the literature: the Endako- and the Climax-type
88 (Selby and Creaser, 2001). The Endako-type deposits are characterised by low-grade
89 (Mo<0.15 wt.%), but large-tonnage Mo ores and low F (<0.05 wt.%) in a continental arc
90 setting associated with calc-alkaline magmatism. Tungsten may be enriched as a by-product
91 metal, but copper occurs as in minor quantities or is absent (Doebrich et al., 1996; Taylor et
92 al., 2012). The Climax-type deposits are instead characterised by high-grade (Mo>0.15 wt.%)
93 Mo ores and high F (>0.05 wt.%) in an intraplate setting and associated with alkali-calcic and
94 alkali magmatism (Westra and Keith, 1981).

95 The duration of the mineralisation process in porphyry systems commonly ranges from
96 100 k.y. to 1.5 m.y. (Sillitoe, 2010). Based on numerical modelling, Cathles et al. (1997)
97 proposed a lifetime no longer than 800,000 years for a geothermal system of temperatures
98 greater than 200 °C. The long lifetime (> 1 m.y.) of magmatic-hydrothermal activity mainly
99 depends upon volume, emplacement depth, and temperature of magma, conductive and
100 convective cooling, and permeability of the host rocks (Taylor et al., 2012). It is also
101 demonstrated that multiple events of magma intrusion can increase the lifetime of porphyry

102 copper deposits in excess of 1 m.y. (Chiaradia et al., 2009; John et al., 2010). The inter-
103 mineral intrusive pulses can be either mineralizing or barren and, consequently, can enrich or
104 destroy the former mineralized zones (Sillitoe, 2010). In particular, long-lived magmatism
105 and fractionation, together with fluid exsolution and a change toward more reducing and acid
106 conditions in the mineralising environment are recognised as the key factors for the Mo
107 endowment in the residual melts (e.g., Candela and Holland, 1986; Keith et al., 1986; Blevin
108 and Chappell, 1992; Candela, 1992; Audetat et al., 2008; Seo et al., 2012; Wilkinson, 2013;
109 Zhang et al., 2018).

110 The majority of the porphyry Cu–(Mo, Au) deposits in Iran occur along the Cenozoic
111 Urumieh-Dokhtar magmatic zone (UDMZ) and the Arasbaran magmatic zone, including the
112 world-class SarCheshmeh, Sungun, and Meiduk deposits (Asadi et al., 2014; Aghazadeh et
113 al., 2015; Richards and Sholeh, 2016) (Fig. 1 and supplementary material #1). The Siah-
114 Kamar Mo deposit (SKMD) (Nabatian et al., 2017b; Simmonds et al., 2019), located at the
115 northwestern termination of the UDMZ, from Mianeh to Hashtroud cities (Figs. 1 and 2), is
116 the only Mo ore reserve in Iran. Despite the presence of some alteration zones, no porphyry
117 deposits or significant mineralisation has been reported in the area before the exploratory
118 studies carried out by National Iranian Copper Industries Company since 2005 (NICICO,
119 2010). Preliminary exploration on the altered zones has shown a significant Mo-W
120 enrichment, whereas the deposit is barren with respect to Cu and Au. The exploration
121 program held by the owner within the SKMD documented the in-depth mineralisation down
122 to 600 m, with a 39.2 Mt proved reserves @ 539 ppm Mo and 66.4 Mt probable reserves @
123 266 ppm Mo (Aria Kansar Samin Co., 2013).

124 Early research studies focused on the magmatism and mineralisation characteristics of the
125 ore deposit. These studies defined the metaluminous, high-K calc-alkaline to shoshonitic
126 geochemical fingerprint of the magmatism referred to a final stage of Neo-Tethys subduction
127 beneath the Iranian plate (Khaleghi et al., 2013; Nabatian et al., 2017b). These studies also
128 reported low salinity and low-to-moderate temperature magmatic fluids as responsible for the
129 mineralisation (Nabatian et al., 2017b). Contrasting age estimates exist for the timing of the
130 Mo mineralisation at the SKMD and still uncertain is the timing and geological scenario of
131 the Mo mineralisation. Nabatian et al. (2017b) presented molybdenite weighted mean Re-Os
132 age of 41.9 ± 3.6 Ma, whereas Simmonds et al. (2019) reported ages between 28.10 ± 0.15
133 and 29.06 ± 0.20 Ma using the same geochronological technique. Simmonds et al. (2019) also
134 reported early Oligocene U-Pb zircon ages (32.70 ± 0.40 Ma to 30.90 ± 0.40 Ma) from the

135 mineralized body, suggesting mineralization has potentially occurred ~1.5 Ma after the
136 crystallization of the porphyry stock. Moreover, key aspects, such as the longevity of the
137 magmatic porphyry system, the hydrothermal-alteration processes, and the structural control
138 on fluid flow and ore mineralisation were poorly considered.

139 Based on detailed field and petrographic investigations integrated with analytical data
140 (fluid inclusion microthermometry, U-Pb zircon, Re-Os Molybdenite, and Rb-Sr
141 geochronology, quartz geochemistry), this contribution is aimed at (i) defining a genetic
142 model for the Mo mineralisation at the SKMD, and (ii) improving our knowledge of the
143 Cenozoic metallogeny within the UDMZ (Fig 1). Our results document an Oligocene, long-
144 lasting history of magma crystallisation/emplacment/alteration (33-28 Ma), which
145 culminated with Mo stockwork mineralisation at ca. 29-28 Ma. The Mo mineralisation was
146 structurally controlled and caused by ore enhancement during renewed magmatism, which
147 induced metal leaching and deposition in the transition from ductile-to-brittle environments
148 above a cooling and degassing magma. These data are used to propose a genetic
149 mineralisation model for the Mo ore and to discuss implications for the regional ore
150 distribution, and for the Mo mineralisation in porphyry systems in general.

151

152 **2. Geological Background**

153 The UDMZ (Fig. 1) records prolonged Cenozoic magmatic activity, spanning from the
154 Paleocene to the Quaternary (e.g., Richards et al., 2006; Chiu et al., 2013; Yeganehfar et al.,
155 2013; Heidari et al., 2015; Ahmadian et al., 2016; Heidarzadeh et al., 2017; Hosseini et al.,
156 2017; Sarjoughian and Kananian, 2017; Shahsavari Alavijeh et al., 2017). A main phase of
157 magmatism occurred during the Eocene-Oligocene, synchronous with the magmatic flare-up
158 at regional scale (Stocklin, 1968; Verdel et al., 2011; Chiu et al., 2013; Moghadam et al.,
159 2016).

160 Based on the mineralisation distribution and types along the UDMZ, a southern and a
161 northern region can be recognised. The southern region, also known as the Kerman Belt,
162 extending from the Naeen city to Bazman volcano (Naeen-Bazman volcanic zone, NBMZ in
163 Fig. 1), hosts the dominant and largest porphyry Cu-Mo deposits of Iran, which are mostly
164 Miocene in age (Aghazadeh et al., 2015). Magmatic products show a general calc-alkaline
165 (moderate to high-K) and metaluminous fingerprint, with a pronounced adakitic signature
166 during the Miocene (Shahabpour and Kramers, 1987; Hassanzadeh, 1993; Shafiei et al.,
167 2008; Taghipour et al., 2008; Shafiei et al., 2009; Mirnejad et al., 2011; Asadi et al., 2014).

168 Three metallogenic stages have been proposed by Aghazadeh et al. (2015) within this
169 segment, including late Oligocene (29–27 Ma), middle Miocene (14–11 Ma), and late
170 Miocene (9–6 Ma). The northern region, extending from Urumieh/BostanAbad to
171 Naeen/Anarak cities (Fig. 1; supplementary material #1), instead hosts a few relatively
172 smaller deposits. Within this region, two magmatic zones can be recognised: (i) a volcano-
173 plutonic zone from BostanAbad to Anarak cities (BAMZ in Fig. 1; supplementary material
174 #1), Eocene to Oligocene in age, typified by high-K calc-alkaline and shoshonitic signatures
175 (e.g., granitoid batholiths of Zanjan, Hassanzadeh et al., 2008; Kal-e kafi, Ahmadian et al.,
176 2009; Abhar, Castro et al., 2013; Kuh-e Dom, Sarjoughian and Kananian, 2017) and
177 associated with some small, intrusion-related, polymetallic deposits (Ahmadian et al., 2009;
178 Fazel et al., 2015; Ahmadian et al., 2016); and (ii) an Oligocene-Miocene volcano-plutonic
179 zone from Urumieh to Naeen (UNMZ; in Fig. 1), which is characterized by post-collisional
180 calc-alkaline and high-K calc-alkaline to adakite products (e.g., Richards et al., 2006; Chiu et
181 al., 2013; Yeganehfar et al., 2013; Babazadeh et al., 2017; Ballato et al., 2017b; Sarjoughian
182 and Kananian, 2017) and associated with minor Au-rich Cu (Mo) porphyry (e.g., Dalli, Ayati
183 et al., 2013) and epithermal Au deposits (e.g., Zarshuran, Mehrabi et al., 1999; Muteh, Moritz
184 et al., 2006; SariGunay, Richards et al., 2006). Regarding the Miocene magmatism, Shafiei et
185 al. (2008) suggested syn- and post-collisional thickening and melting of Cu- and sulfur-rich
186 peridotite, near the crust–mantle boundary, as responsible for fertile adakitic magmatism in
187 the southern Urumieh-Dokhtar magmatic zone. In contrast, Haschke et al. (2010) suggested
188 that a syn- or post-collisional Miocene delamination in the northern UDMZ had removed the
189 Cu- and S-enriched metasomatised lithospheric arc-root and, subsequently, prevented the Cu
190 mineralisation during collisional magmatism.

191 The AMZ is adjacent and sub-parallel to the UDMZ, running from the Sabalan
192 volcano to the Jolfa city, probably continuing to Armenia into the lesser Caucasian Magmatic
193 zone (Innocenti et al., 1982; Hassanpour et al., 2014; Simmonds et al., 2017) (Fig. 1). The
194 AMZ boundaries have not been defined yet, although it is normally considered as a segment
195 of the UDMZ. Nonetheless, it has been also considered as a part of western Alborz zone
196 (Nabavi, 1976; Aghanabati, 2004; Moritz et al., 2016; Rolland, 2017). The porphyry Cu (Mo-
197 Au) mineralisation span from Oligocene to early Miocene (e.g., Shahabpour and Kramers,
198 1987; McInnes et al., 2003; Aghazadeh et al., 2015) and it is more intense with respect to the
199 northern region of the UDMZ.

200

201 3. Materials and Methods

202 A multidisciplinary research approach is adopted in this study that includes field work
203 and laboratory analyses. Field work was based on the existing 1:250,000 cartography (Amidi
204 et al., 1987) and addressed to map the main magmatic bodies and the alteration types (Fig. 2).
205 A detailed map at the scale 1: 5000 is produced for describing the alteration zoning and the
206 main ore zones (Fig. 3). Field work and petrographical observation form the basis for the
207 sampling strategy for the laboratory work that includes: (i) fluid inclusion microthermometry,
208 (ii) Raman spectroscopy; (iii) LA-ICPMS trace and rare earth (REE) elements analysis; (iv)
209 zircon U-Pb geochronology; (v) molybdenite Re-Os geochronology; and (vi) multi-mineral
210 Rb-Sr geochronology of the alteration assemblages.

211 The studied samples are shown in Figure 3 and listed in Table 1, where their location,
212 petrography and analytical methods adopted are detailed. The analytical protocols are
213 described in the Appendix. In the following, mineral abbreviations are after Whitney and
214 Evans (2010).

215 216 4. Geology of the study area and the ore deposit

217 The SKMD is located within the Mianeh intermountain basin (Heidarzadeh et al., 2017),
218 in-between the Alborz and the AMZ, at the southern margin of the Azerbaijan Block at the
219 tip of the active dextral Tabriz Fault (Figs. 1, 2). The stratigraphy of the area is dominated by
220 a wide exposure of Eocene volcanic rocks, which make-up the country rocks of the SKMD.
221 The Eocene volcanic rocks consist of andesite-basalt and trachy-andesite lava beds and vitric
222 dacitic to andesitic tuff (Amidi et al., 1987) (Fig. 2). These volcanic products are intruded or
223 covered by a composite Cenozoic (Oligocene-Miocene) volcano-plutonic complex (Amidi et
224 al., 1987; Khodabandeh et al., 1999). A variety of intrusive and sub-volcanic rocks with
225 variable geometry and composition occur in the study area, including diorite, monzonite to
226 leuco-granite, and rhyodacite porphyry (Amidi et al., 1987; Khodabandeh et al., 1999). The
227 granular intrusive bodies crop out in the northwest and centre of the study area, generally
228 aligned along a NW-SE orientation (Fig. 2). To the southeast (from Khatoon Abad to Siah-
229 Kamar), an array of E-W to NE-SW striking microgranular and porphyritic felsic stocks and
230 dykes crop out (Fig. 2). Miocene volcanic country rocks consist of tuff and ash layers with
231 interlayered andesitic lava beds. This volcanic succession is covered by upper Miocene
232 continental sedimentary deposits (Upper Red Fm.) that crop out in the northwestern and
233 southwestern sectors of the study area. These deposits are unconformably covered by

234 Pliocene-Quaternary continental sedimentary successions (Amidi et al., 1987; Ballato et al.,
235 2017a) (Fig. 2).

236 The ore deposit geology is characterised by a major alteration zone centered on a
237 porphyry-type, composite magmatic complex that, intruded within the Eocene volcanic rocks,
238 hosts the main Mol ore (Figs. 2 to 4). Despite the different alteration types, the magmatic
239 bodies share common textural features consisting of a porphyritic microgranular and/or
240 glassy groundmass, with various proportions of AFs, Pl, and mafic phenocrysts (Cpx and/or
241 Amp) in the primary igneous assemblage (see Table 1 for a detailed description). Based on
242 the estimated modal abundance of the primary igneous mineral components, the rock
243 compositions are andesitoid/basaltoid (Le Maitre et al., 2005). The mineralized porphyry
244 body (samples MN02 and MN03 in Table 1) is the largest stock in deposit area with a NW-
245 trending ellipsoid shape (1800×1300 m). The body experienced intense alteration and in
246 some places the primary texture has been destroyed. Where preserved, the primary rock
247 composition ranges from syenite to monzonite-quartzmonzonite (Nabatian et al., 2017b).
248 Also barren magmatic bodies can be recognised in the area, to the south (sample MN31 in
249 Table 1) and to the north (sample MN65 in Table 1) of the mineralised body, in a continuum
250 from syn-to-post ore stage as documented by the alteration patterns and distribution (see inset
251 in Fig. 3).

252 Based on the mapped outcrops of alteration zones and assuming lateral continuity below
253 the Miocene and Pliocene cover rocks, the reconstruction of the alteration zone shows an
254 ellipsoid shape, with a general NW-SE trend and about 4×3 km of areal extent (Fig. 3). The
255 Mol mineralisation occurs both as minor disseminated within the inner potassic-sodic
256 alteration zone and major focused in Qz-Afs-Cb veins.

257 A suite of acidic subvolcanic products (rhyolitic and dacitoid in composition; samples
258 Mn01 and Mn19 in Table 1) are observed to intrude and post-date the alteration zone. These
259 magmatic rocks show only minor evidence of rock alteration (Fig. 3; Table 1).

260

261 **5. Alteration types**

262 Alteration zoning grades from potassic-sodic alteration in the centre to adjacent phyllic
263 and peripheral propylitic halos (Fig. 3). In the following, we described the main alteration
264 zones, mineral assemblages and their distribution.

265 **5.1. Potassic-sodic alteration**

266 The potassic-sodic alteration is observed in the core of the altered zone, with an areal
267 extent of ca. 2.4 km² (Figs. 3, 4). The alteration is typified by the mineral assemblage Bt+ Kfs
268 + Ab + Mag + Anh ± Ilm, Ap, Mol. Typical is the occurrence of a secondary spotted texture
269 made of Bt-Mag aggregates, likely overprinting early magmatic layering (Fig. 5a). Secondary
270 anhedral Kfs and Ab aggregates overprint early magmatic Pl (Fig. 5b). Molybdenite typically
271 occurs as disseminated flakes within the alteration matrix (Fig. 5c). Biotite occur as very fine
272 grained, dominantly as disseminated grains but also as irregular curvy vein-like aggregates
273 (Fig. 5d). Magnetite grains occur both as fine-grained disseminated crystals in the
274 groundmass and as inclusion in Kfs (Figs. 5b, e). Minor amount of Ilm is observed as
275 inclusions in Bt (Fig. 5e). Late formed Po veins also occur (Figs. 5d). Stockwork
276 development and partial brecciation are ubiquitous and resulted in diverse vein types (Fig. 5a;
277 see also below).

278 **5.2. Propylitic alteration**

279 Propylitic alteration is the largest alteration zone that mainly affects the Eocene volcanic
280 host rocks and the porphyry-type magmatic complex (Figs. 3, 4). The width of the propylitic
281 alteration is at least 1 km, but it suddenly decreases with distance from the porphyry-type
282 magmatic complex. This alteration is typified by the assemblage Ep ± Act ± Cb ± Py with
283 stockwork, disseminated and locally brecciated textures close to the porphyry-type magmatic
284 complex (Fig. 5f).

285 **5.3. Phyllic alteration**

286 The phyllic alteration rims the core of the potassic-sodic and the marginal alteration zone.
287 Locally it overprints the inner part of the potassic alteration zone (Figs. 3, 4). The phyllic
288 alteration consists of the assemblage Qz + Mus + Py, which is variable distributed within the
289 alteration zone, usually associated with veining and rock fractures, seldom associated with
290 intensive pyritization (ca. 5- 10 % vol.). Pyrite is typically altered to secondary iron oxide and
291 hydroxide minerals in the uppermost portions of the alteration zone. Intermediate argillic
292 alteration (Sillitoe, 2010) is observed to decorate the damage zone of major faults (Fig. 5g-j).

293 **6. Veining**

294 We documented multistage veining, locally associated with pronounced alteration halos.
295 The vein density is highly variable and commonly decreases toward margins of the alteration
296 zones, where the alteration distribution is mainly influenced by vein distribution and
297 persistence. In particular, the vein volume abruptly interrupts at the boundary between the
298 mineralised porphyry complex and the Eocene volcanic host rocks (Fig. 6a).

299 Azimuth rose diagram generated from the measured cumulative vein strikes reveals a
300 mean E-W orientation, associated with minor NW-SE and N-S ones (Fig. 6b). In the
301 following, a description of the vein texture and assemblages is described for each alteration
302 zone.

303 **6.1. Veins in the potassic-sodic alteration zone**

304 A conceptual scheme of the vein generation at the microscale within the inner potassic-
305 sodic zone is presented in Figure 7. The early veins generation (V1) consists of up to mm-
306 size Bt and minor Qz+Po, Ab+Kfs and Kfs veins, sharing a discontinuous and irregular curvy
307 shape. The Fsp veins are commonly associated with Fsp halos; no evidence of Mol
308 mineralisation is observed. Locally, small (up to 0.5 mm) curvy shapes Qz ± Po veins are
309 also observed (Fig. 5d).

310 The second generation (V2a) consists of a voluminous, cm-sized, Qz-Kfs ± Mol ± Ab non-
311 systematic (stockwork) vein array (Figs. 5a and 8a-c). These veins are characterized by a
312 blocky texture, mainly formed by Qz-Kfs aggregates, commonly associated with minor Mol,
313 Sch, and Rt (Figs. 7 and 8a,c). The overall vein texture suggests syntaxial growth and Mol
314 occurs in equilibrium with Qz (Figs. 7 and 8a,b). Carbonate mineralisation is typified by the
315 early appearance of paraspurite ($\text{Ca}_5(\text{SiO}_4)_2\text{CO}_3$) (Colville and Colville, 1977), and Ank and
316 Sid/Ank in the stage-2 veins, which occurs in the vein suture, likely filling remaining vugs
317 (Fig. 8).

318 The third generation (V2b) corresponds to the main ore stage and is characterised by Cb-
319 Mol veins, associated with minor sericite and pyrite (Fig. 9). The Cb-Mol veins mostly
320 rework the pre-existing Qz-Fsp veins/host rocks contacts, often developed as cross-cutting
321 and inter-granular cracks (Fig. 9 a,b). Locally, brecciation of the early Qz-Fsp veins is
322 observed, associated with massive Mol precipitation that often show rosette texture (Figs.
323 9a). A ribbon appearance is commonly observed in the V2b veins due to alternating variation
324 of Cb minerals (Fig. 9c). It is worth nothing that Cb compositions vary from Cal to
325 Sid/Rds/Ank when in equilibrium with the Mol precipitation (Fig. 9b,c). Muscovite mostly
326 developed at the expenses of pristine Kfs (Fig. 9d).

327 In terms of vein distribution, the overall array of Mol mineralised veins (V2a-V2b) is non-
328 systematic (Fig. 6c). When taking into account the V2b vein array, a more systematic
329 distribution is observed, which cluster along the E-W (dominant) and NS strikes (Fig. 6d).

330 **6.2. Veins in the propylitic alteration zone**

331 The propylitic zone is associated with development of brecciation and veins, close to the
332 porphyry mineralised body and in the distal country rocks, respectively. Brecciation causes

333 fragmentation of the country rocks, cemented by Ep+Act+Cb aggregates. Veins occur as
334 high-angle systematic arrays, striking roughly E-W and N-S (Fig. 6e), and are filled with the
335 same mineralogical assemblage (Ep+Act+Cb).

336 **6.3. Veins in the phyllic alteration zone**

337 Within the phyllic alteration zone, veins are made of mm-size Qz + Py, associated with
338 sub-mm-size Ms (sericite) halos (Fig. 5g-j). They form non-systematic arrays. Within the
339 higher topographic levels of phyllic alteration, the Py grains are converted to iron oxide and
340 hydroxide minerals.

341

342 **7. Mo ore mineralisation**

343 Two main stages of Mol mineralisation were recognized either as disseminated or
344 stockwork (Figs. 9 and 10). Stage-1 (Mol-I) occurs as disseminated Mol flakes within the
345 porphyry body, in association with the potassic-sodic alteration (Fig. 5c). Stage-2 can be
346 subdivided in two Mol formation events (stage-2a and -2b in Figs. 9 and 10), Mol-II and
347 Mol-III, respectively. Mol-II occurs during V2a formation, in association with minor Sch and
348 Rt. Mol-III is the high-grade ore stage during the Cb V2b formation, beginning with
349 parasporite and continuing with Fe-Mn Cb mineralisation. Minor amount of Py and
350 secondary Ms (sericite) are associated with the Mol-III precipitation.

351

352 **8. Quartz chemistry and Ti-in quartz thermometry**

353 Quartz crystals from V2a veins from the potassic-sodic alteration zone were analyzed by
354 in situ LA-ICP-MS for Ti content (16 grains) and trace elements (7 grains). Results are
355 presented in Table 2 and 3, respectively. Analytical details are provided in the Appendix.

356 Analyzed quartz show high Ti (17.4-54.7 ppm) and Al (35.9-160.2 ppm), with significant
357 enrichment in Li (1.9-28.0 ppm) and Ge (0.9-2.0 ppm). In the Al vs. Li diagram, the analysed
358 quartz grains show positive correlation and fall near the 1:1 Al/Li molar ratio line, which is
359 indicative of magmatic and hydrothermal quartz (Dennen, 1966; Müller et al., 2018). In the
360 Al vs. Ge diagram, the quartz compositions are compatible with those from hydrothermal
361 quartz and the Ti contents are typical of quartz veins from (Mo-Cu-Au)-porphyry-type
362 deposits (e.g., Müller et al., 2018) (Fig. 11).

363 The TitaniQ thermometry (Wark and Watson, 2006; revised by Huang and Audétat, 2012),
364 assuming a $a_{TiO_2} = 1$ for rutile-present conditions provides temperature estimates of 479-575
365 ± 50 °C and 568-675 ± 50 °C at 0.5 and 2.5 kbar, respectively.

366

367 **9. Fluid-Inclusion Study**

368 **9.1. Petrography**

369 Samples from (i) Qz-Fsp V2a and Cb-Mol V2b veins from the potassic-sodic alteration
370 zone (Fig 9a) and (ii) Qz-Py-Ms veins from the phyllic alteration zone (Fig. 5i) were studied
371 for fluid inclusions (FI) analysis in order to assess the chemical-physical properties of the
372 mineralising fluid(s). FI were measured both in quartz and paraspurite from the same vein
373 assemblage, considered as representative of the main Mol mineralisation stages.

374 Based on the observed phases at room temperature, two main types of aqueous FI were
375 recognised following the classification proposed by Roedder (1984): (i) dominant type-A (L-
376 rich + V); and (ii) minor, solid-bearing, type-B (L-rich + V + solid). Type-A is subdivided
377 into four sub-groups based on the alteration zone, host mineral and the V to L volume ratio,
378 from A1 to A4. A summary of FI characteristics and results are given in Table 4. The various
379 identified FI types in this study are briefly described below. Type-A1 and A2 are L-rich + V
380 FI, found within V2a quartz grains in the potassic-sodic alteration zone with the V to L ratios
381 from 0.5 to 1 and from 0.1 to 0.4, respectively. Type-A3 are L-rich + V FI. They are the only
382 detected FI inside quartz crystals from Qz+Py+Ser veins within phyllic alteration zone. Type-
383 A4 are L-rich + V FI from V2b paraspurite crystals within the potassic-sodic alteration zone.

384 Type-A1 are mostly found as solitary or randomly distributed in well-protected Qz grains
385 form post entrapment shearing, and have regular to subhedral geometry, large size (ranging
386 15-100 μm). They occasionally show negative crystal shape, and possess the highest V to L
387 ratios (Fig 12a). Type-A2 FIs are characterized by small sizes (5 to 20 μm), regular with
388 negative crystal shape to irregular geometry (Fig 12b). Type-A3 are very similar to type-A2
389 FI, but with smaller sizes (ranging 5 to 10 μm). They have regular to irregular shapes, some
390 showing negative crystal shapes and their V to L ratios range from 0.2 to 0.4 (Fig 12c). Type-
391 A4 occur along the cleavages of the host crystal, showing irregular and elongated geometry
392 with sizes range 5-20 μm . The V to L ratios range from 0.1 to 0.25, but commonly are below
393 0.15 (Fig 12d).

394 Type-B are solid-bearing L-rich + V FI, rarely found in the cores of V2a quartz grains (Fig
395 12e). They occur mainly isolated and in confined trails that are interpreted to be quartz
396 growth lines. Their sizes range 15-30 μm and mostly have irregular geometry. Their V to L
397 ratios range from 0.1 to 0.2.

398 **9.2. Raman Spectroscopy**

399 Raman spectroscopy was utilized to define the composition of V and L phases of the type-
400 A FI. For the types-A1 and A4 FI, the obtained spectra for the L and V phase revealed water
401 and water vapor as the major components, respectively (Fig 13). In addition, the L phase of
402 type-A1 FI also showed a clear peak for CO₂ (at 1384 cm⁻¹) in solution (Fig 13a). Other
403 peaks were too weak and not identified. In the V phase of type-A1 FI, apart from water
404 vapor, the only detected gas component is CO₂ (Fermi doublet at 1285 and 1388 cm⁻¹). A
405 weak peak belonging to CO₃²⁻ (1064 cm⁻¹) was also detected (Fig 13b).

406 The results from parasprite-hosted type-A4 FI were not so clear due to the strong
407 fluorescence of the hosting mineral. No evidence of gases were detected.

408 9.3. Microthermometry

409 A summary of the FI micro thermometric data is reported in Table 4 and histograms of
410 salinity and T_h are illustrated in Figure 14. All the FI types homogenized to L. The eutectic
411 temperatures (T_e) for the type-A1 FI range -30 to -22.5 °C (mean of -25.3 °C), which are
412 higher than eutectic temperature for the H₂O-NaCl system (Bodnar, 1993). The minimum
413 recorded T_e could be considered as the ternary eutectic point temperature (-23 °C) of the
414 H₂O-NaCl-KCl system (Hall et al., 1988). Since minor amounts of CO₃²⁻ was detected by
415 Raman spectroscopy studies inside type-A1 FI, the higher recorded T_e values could be
416 explained by the presence of variable amounts of other components, such as Na₂CO₃
417 (K₂CO₃?) in addition to NaCl and KCl. The final ice-melting (T_{m-ice}) temperatures range from
418 -3.7 to -0.6 °C ($n = 44$), which corresponds to salinities between 6.85 and 1 wt.% NaCl eq.
419 (with a mode of 3.85 wt.% NaCl eq). Type-A1 shows the highest homogenisation
420 temperature (T_h) estimates, ranging 298-365 °C and a well-defined mode at 340 °C (mean
421 value of 333 °C). These values are similar to those obtained by Nabatian et al. (2017b) on the
422 same FI type.

423 The T_e for the type-A2 FI range -31.5 to -23°C, with a mode at -23 °C, compatible with
424 the ternary eutectic point temperature of the H₂O-NaCl-KCl system (Hall et al., 1988). The
425 higher recorded values suggest the presence of other components as for type-A1. The T_{m-ice}
426 ranges from -3.7 to -0.1 °C ($n = 195$), which correspond to salinities between 6.0 and 0.18
427 wt.% NaCl eq., with a mean of 2.6 wt.% NaCl eq.. The T_h values distribute almost
428 homogeneously in a wide range from 170 to 352 °C, with a mean at 272°C.

429 Due to the small size of type-A3 FI, the T_e were measured only in two cases, which
430 provided -22 and -21 °C, respectively. The obtained values are close to the eutectic point
431 temperature of H₂O-NaCl system. The T_{m-ice} ranges from -2.6 to -1 °C ($n = 52$), which
432 correspond to salinities between 4.3 and 1.7 wt.% NaCl eq., with a mean of 1.8 wt.% NaCl

433 eq. The T_h values range 232-365 °C, but the data are skewed to higher temperatures, with a
 434 mode at 310 °C.

435 The T_e for the type-A4 FI range -33 and -24 °C, with a mean of -27 °C. Since these FI are
 436 hosted in carbonate minerals, these T_e values can be attributed to the presence of CO_3^{2-} and/or
 437 ions such as Ca^{2+} , Mg^{2+} , Fe^{2+} in addition to $\text{H}_2\text{O}+\text{NaCl}$ in the fluid. The $T_{m\text{-ice}}$ ranges from -
 438 1.2 to -0.1 ($n = 91$), which correspond to salinities between 2.1 and 0.2 wt.% NaCl eq., with a
 439 mean of 0.6 wt.% NaCl eq. The T_h values are distributed in a very wide range, from 145 to
 440 300 °C, with a well-defined mode at 225 °C.

441 The salinity estimates for type-B FI were calculated only in four FI from the melting
 442 temperature of halite in the liquid phase upon heating. Halite crystals disappeared prior to the
 443 bubble in all FI. The calculated salinity estimates range from 30.5 to 32 wt.% NaCl eq. The
 444 average T_h spreads between 203 and 320 °C.

445

446 **10. U-Pb zircon dating of magmatic rocks**

447 The zircon U-Pb geochronological study was carried out on zircon separates as obtained
 448 both from the mineralised (sample MN03) and barren magmatic rocks (samples MN01,
 449 MN19 and MN31; Fig. 3 and Table 1). Few zircon grains were recovered from the
 450 andesitoid/basaltoid rocks (MN03 and MN31), whilst the acidic rocks (MN01 and MN19)
 451 provided a large number of grains. Zircons were first investigated through
 452 cathodoluminescence (CL), and back scattered electron (BSE) imaging techniques and then
 453 analysed in situ LA-ICP-MS system at the university of Nagoya, Japan (see the Appendix for
 454 the methodology and). Analytical results are summarized in Table 5.

455 ***MN03***

456 Zircons are generally euhedral to subhedral. Zircon grains show short to long prismatic
 457 habits (usually $>100 \mu\text{m}$ up to $500 \mu\text{m}$), with length/width ratios 2:1 and up to 6:1. Most of
 458 the grains appear as nearly homogeneous in BSE images with rare brighter cores. Most of
 459 them possess a few continuous longitudinal fractures and apatite and feldspar inclusions are
 460 common. The CL images show oscillatory to sector growth zoning (Fig. 15a). The Th/U
 461 values are in the range 0.38-6.3 ($n = 21$; Table 5), compatible with an igneous origin (e.g.,
 462 Rubatto, 2002; Kirkland et al., 2015). Despite discordance of some of the spot results due to
 463 Pb loss, the majority of the data define a nearly concordant cluster at about 33 Ma. In a Tera-
 464 Wasserburg Concordia diagram, an intercept age of $32.8 \pm 1.1 \text{ Ma}$ is obtained (2σ ; MSWD =
 465 3.5, $n= 13$) (Fig. 15b).

466 **MN31**

467 Most of the zircon grains are of small size (50 to 150 μm) and can be classified as type-1
468 subhedral to anhedral and type-2 euhedral crystals. Type-1 shows complex growth zoning
469 with marginal resorption. Type-2 show oscillatory growth zoning (Fig. 15c). The Th/U values
470 range between 0.3 and 2.57, attesting a magmatic origin. Age analyses of type-1 zircons
471 reveals a large spread in apparent $^{206}\text{Pb}/^{238}\text{U}$ ages from 41.1 ± 1.6 to 2611 ± 70 Ma (Table 5).
472 Type-2 zircons yielded the youngest apparent $^{206}\text{Pb}/^{238}\text{U}$ ages at ca. 30 Ma, with a Concordia
473 age of 30.4 ± 1.2 Ma (2σ ; MSWD = 0.12, n= 2) (Fig. 15d).

474 **MN01**

475 Zircon grains are generally euhedral to subhedral and show short to medium prismatic
476 habits (usually >100 μm up to 250 μm), with length/width ratios of around 2:1. Most of the
477 grains host abundant inclusions of Ap, Fsp, and Qz. The grains show heterogeneous zoning in
478 BSE images with oscillatory and sector growth zoning in CL images. Xenocrystic cores are
479 rarely preserved, and the cores are overgrown by oscillatory and sector zoned rims (Fig. 15e).
480 Th/U values are systematically above 0.4. The majority of the apparent zircon $^{206}\text{Pb}/^{238}\text{U}$ ages
481 from the growth zoning domains cluster at about 29 Ma, with a few grains providing early
482 Cambrian (ca. 529 Ma) to the Upper Triassic (ca. 220 Ma) ages. A Concordia age of $28.9 \pm$
483 0.4 Ma (2σ , MSWD = 1.2; n=15) is obtained from the Oligocene zircon population (Fig.
484 15f).

485 **MN19**

486 Zircon grains are generally euhedral to subhedral and show short to long prismatic habits
487 (usually >100 μm up to 300 μm), with length/width ratio of 2:1 to 3:1. Most of the grains
488 are heterogeneous and inclusion bearing in BSE images and some of them contain
489 xenocrystic cores. In CL images, most of the grains show oscillatory and sector zoning in rim
490 domains (Fig. 15g). The measured Th/U values are higher than 0.4. Most of the spots
491 performed on the growth domains provided concordant ages, with a Concordia age of $28.3 \pm$
492 0.4 Ma (2σ , MSWD = 0.68; n=21) (Fig. 15h).

493

494 **11. Molybdenite Re-Os geochronology**

495 Two molybdenite-bearing samples were collected from V2b high-grade Mol veins (stage-
496 2b mineralisation) from the core of the potassic alteration zone (Fig. 3 and Table 6) for Re-Os
497 Mol geochronology (see Appendix). The two samples possess similar Re abundances (~ 19.3
498 and 22.1 ppm), and as they yield very similar Re-Os dates (below) also contain similar ^{187}Os

499 abundances (~12.2 and 13.9 ppb). The two samples yielded similar Re-Os dates of 28.3 ± 0.2
500 and 28.7 ± 0.2 Ma (Table 6). These ages are in excellent agreement with those previously
501 presented for the SKMD (ca. 29 – 28 Ma) by Simmonds et al. (2019), but are in contrast with
502 much older reported Re-Os Mol dates (ca. 42 Ma) by Nabatian et al. (2017b). The Re-Os Mol
503 dating results of this study and those of Simmonds et al. (2019) also overlap with the U-Pb
504 zircon ages (ca. 29-28 Ma) of the acidic magmatic bodies (samples MN01 and MN19) that
505 intrude the main alteration zone (Fig. 3).

506

507 **12. Rb -Sr geochronology of the alteration zone(s)**

508 Several samples were selected for Rb-Sr geochronology in order to constrain the age of
509 the fluid-driven alteration processes within the SKMD. Only sample MN02 (rock matrix)
510 coming from the inner potassic-sodic alteration zone provided reliable results (see Table 7,
511 Fig. 16). In other samples either Rb/Sr values of minerals like sericite or Kfs were too low to
512 facilitate derivation of useful age information, or samples were affected by supergene
513 alteration. Results for these samples will be reported elsewhere.

514 For sample MN02, the mineral assemblage in the matrix consists of the early-stage
515 alteration products made of Kfs + Bt + Ap with minor amounts of Mol and Qz. Lately formed
516 Ms (sericite) is also documented. We analyzed Bt, two grain size fractions of Kfs, Ap, and
517 two grain size fractions of sericite. The age obtained for the primary assemblage Bt+ 2
518 Kfs+Ap is 33.3 ± 0.9 Ma with a MSWD (mean square weighted deviation) of 0.16,
519 documenting that this sub-assemblage was in perfect Sr-isotopic equilibrium at that time. The
520 late-stage Ms was formed by fluid-rock interaction and most probably grew at the expense of
521 primary Kfs. Linear regression of the Rb-Sr data for 2 Kfs + Ap +2 Ms results in an age of
522 28.5 ± 1.8 Ma (MSWD = 6.3). It appears that there is slight Sr-isotopic disequilibrium
523 between the two different grain size fractions of sericite, which slightly deteriorates the
524 precision of the age but does not affect its accuracy.

525

526 **13. Discussion**

527 The zircon U-Pb geochronology from the ore-related intrusive bodies points to a
528 multistage magma emplacement in the study area that, based on the petrographic
529 characteristics, can be grouped in two main episodes of magmatism, at 33-30 Ma (basic to
530 intermediate in composition) and at ca. 29-28 Ma (acidic in composition), respectively. The

531 early episode of magmatism is compatible with the early Oligocene U-Pb zircon ages
532 reported in Simmonds et al. (2019) on the same mineralised body.

533 These magmatic episodes are associated with chronologically distinct
534 alteration/mineralisation types, as discriminated by the Rb-Sr multiminerals and Re-Os Mol
535 geochronology. In particular, the Rb-Sr geochronology documented an early Bt-Kfs-Ap
536 assemblage at ca. 33 Ma and a subsequent Ms-bearing one at ca. 28 Ma, thus coeval with the
537 early basic and late acidic magmatic episodes, respectively. We can thus infer the two-stage
538 Mo mineralisation as defined by the textures and mineralogical assemblages in the SKMD
539 (Fig. 10) was polyphase and the consequence of : (i) an early low-grade, disseminated-type
540 mineralisation (stage-1) at ca. 33 Ma, associated with the pervasive potassic-sodic alteration
541 during basic to intermediate magmatism; and (ii) a subsequent, high-grade focused stockwork
542 mineralisation (stage-2) at ca. 29-28 Ma, associated with Qz-Fsp veining and subsequent Cb
543 precipitation during acidic magmatism. This evidence suggests a long-lived (at least 4-5 Ma)
544 period of magma production, differentiation and emplacement to sustain the Mo
545 mineralisation episode(s) in the study area.

546 To form an economic porphyry Mo mineralisation, a significant and multiple magma
547 supply and differentiation within a large magma chamber, is needed to endow reasonable
548 quantities of Mo (e.g., Candela and Holland, 1986; Candela, 1992; Robb, 2004; Audétat,
549 2010; Zhang et al., 2018). The lack of Cu mineralisation in the SKMD, which is at odds with
550 the all known porphyry systems along the Urumieh-Dokhtar magmatic zone (supplementary
551 material #1), also supports a scenario of a long-lasting magma crystallisation and
552 differentiation in the chamber(s), which efficiently led to Cu extraction from the melt to the
553 crystallizing marginal zones into sulfide minerals (e.g., Candela and Holland, 1986; Blevin
554 and Chappell, 1992; Candela, 1992; Klemm et al., 2008; Audétat, 2010). The residual melt
555 magma from such a chamber is then expected to show depletion in Cu and relative
556 enrichment in Mo. With progressive crystallization, a more acidic, fluid-rich magma is
557 produced which would be more fertile with respect to Mo (e.g., Candela and Holland, 1986;
558 Candela, 1992; Robb, 2004; Audétat, 2010; Seo et al., 2012).

559 The longevity of magma chamber(s) could be simply related to the amount of primitive
560 magma nesting deep in the crust (Hawkesworth et al., 2000), the water content of the magma
561 that prevented magma to rise to the same crustal levels unlike its drier equivalent (Robb,
562 2004), or input of numerous batches of magmas from the deep crustal melt reservoir (Glazner
563 et al., 2004).

564

565

566 **13.1. Source of the Mo-bearing magma**

567 Apparently, there is a good correlation between Re concentration values in Mol and source
568 of the parental magma. In particular, high (hundred ppm) and low (few ppm) Re contents
569 have been reported in many studies and were referred to as mantle- or to crust-derived
570 magmas, respectively (e.g., Stein et al., 2001; Berzina et al., 2005; Mao et al., 2006; Wu et
571 al., 2017). However temperature of Mol deposition (Ishihara, 1988), the alteration type within
572 the same deposit (Newberry, 1979), and the availability of molybdenite could affect the
573 amount of Re concentrations. Furthermore, based on Nd and Sr isotopic studies, Farmer and
574 DePaolo (1984) proposed that the Cu source is in the mantle and the Mo source in preexisting
575 crust. Many studies have also documented that the most fertile sources for syn- and post-
576 collisional porphyry deposits is a subduction-modified lithosphere (Pettke et al., 2010;
577 Richards, 2015).

578 Molybdenite samples from Tertiary porphyry deposits in Iran show a general positive
579 correlation between higher Re concentration and younger ages (Taghipour et al., 2008;
580 Mirnejad et al., 2013; Aghazadeh et al., 2015; Simmonds and Moazzen, 2015; Nabatian et al.,
581 2017a; 2017b). It was therefore proposed that the Neogene magmas along UDMZ were less
582 contaminated by crustal materials (Nabatian et al., 2017b).

583 The Re contents in the molybdenite samples analysed in this study (19-22 ppm), together
584 with those presented in Simmonds et al. (2019), ranging 10-41 ppm, are remarkably lower
585 than all other porphyry Cu-Mo (Au) systems along the Urumieh-Dokhtar magmatic zone,
586 which are typically above 100 ppm (e.g., Aghazadeh et al., 2015). Significant in this regard is
587 the presence of inherited zircons within both the early (dated at 33-30 Ma) mafic to
588 intermediate and late (dated at 29-28 Ma) acidic magmatic rocks cropping out in the
589 mineralised area (Table 5). These inherited zircons also show resorbed and heterogeneous
590 textures (Fig. 15d), compatible with renewed melting and corrosion (Corfu et al., 2003). In
591 this regard, various papers have outlined the dominant role of juvenile lower crust in metal
592 endowment in porphyry Mo (e.g., Berzina et al., 2015; Liu et al., 2015; Zeng et al., 2015;
593 Zhang et al., 2018) and Cu deposits along southern UDMZ (Asadi et al., 2014). We therefore
594 suggest that the molybdenite Re contents from the SKMD most likely derive from a crustally-
595 contaminated mantle sourced magma. This is in line with the calculated initial isotopic Sr
596 composition of ~ 0.70497 as derived from sample MN02 (Fig. 16) that is indicative of a
597 mantle-derived magma with minor crustal contaminations (Zindler and Hart, 1986).

598

599 **13.2. Structural control on fluid flow and mineralisation**

600 The Mo mineralisation SKMD is structurally controlled as documented by the
601 development of a network of polyphase veining. Overall, the vein arrays are non-systematic,
602 as indicated by a nearly radial pattern of jointing within the main alteration zones (Fig. 6b-c),
603 and the Mol abundance in veins (V2a and V2b) decrease significantly when moving from the
604 inner potassic-sodic alteration zone focused on the main intrusive body to the outer Eocene
605 volcanic host rocks (Fig. 3). Similarly, the intensity of the phyllic alteration changes from
606 intense to low when crossing the contact between the mineralised porphyry and the volcanic
607 host rocks. This evidence suggests that the original intrusive contacts constituted a major
608 structural/rheological boundary that likely acted as a permeability barrier for the fluids
609 exsolved from the crystallizing intrusion (e.g., Oliver and Bons, 2001; Rossetti et al., 2007).

610 Significantly, within the ore body the vein array is more systematic in the transition
611 from V2a to V2b mineralisation stages and in the marginal propylitic alteration zone (Fig. 6).
612 In particular, the occurrence of a nearly orthogonal vein set in the potassic-sodic and
613 propylitic alteration zones points to a geological setting dominated by a horizontal biaxial
614 tensile stress field in an extensional regime (vertical maximum principal stress σ_1) and
615 characterized by reversal of the intermediate (σ_2) and minimum (σ_3) principal stress (Rives et
616 al., 1994; Caputo, 1995) between the NS and E-W paleo-directions. Since the main vein
617 strike distribution cluster around the E-W strike (Fig. 6), the regional σ_3 paleo-direction
618 during the main stage of Mol mineralisation is inferred to trend NS. Therefore, a transition
619 from a nearly isotropic stress field to a differential stress regime dominated by a N-S directed
620 σ_3 direction is envisaged. This also suggests a different style of structural control on ore
621 mineralisation, likely controlled by the fluid pressure changes in the mineralising
622 environment: from early hydrofracturing and stockwork vein arrays under supralithostatic
623 fluid pressures conditions to late planar vein arrays formation under sub-lithostatic
624 conditions.

625 **13.3. Fluid evolution and the mineralising environment**

626 No information is provided in this study regarding the fluid(s) geochemistry
627 responsible for the main potassic-sodic alteration and associated disseminated stage-1 Mol
628 precipitation. The main products of this stage fluid(s) (as disseminated and micro-vein types)
629 are Kfs+Ab+Bt+Mt+Po, which is the common high-temperature mineral assemblage in the
630 early stages (orthomagmatic) of porphyry systems (e.g., Shinohara et al., 1995; Seedorff et

631 al., 2005; Sinclair, 2007; Sillitoe, 2010), including Mo deposits (e.g., Questa, Bloom, 1981;
632 and Hudson Bay Mountain, Klemm et al., 2008). This is in line with the compositional
633 layering in the porphyry stock (Fig. 5a), which suggests magma degassing close to the
634 carapace of the rising intrusive body (Sinclair, 2007; Lawley et al., 2010). A magmatic origin
635 for this stage-1 fluids is thus tentatively proposed indicated by the ubiquitous unidirectional
636 solidification textures observed in potassic-sodic alteration zone as it proposed at MAX
637 (Lawley et al., 2010) and Henderson (Shannon et al., 1982) porphyry Mo for the early stage
638 fluids (Lawley et al., 2010). The transition from an oxidising to a reducing mineralising
639 environment is attested by the sequential formation of magnetite, to ilmenite and pyrrhotite
640 (Fig. 10), which can be associated to the Mol-I disseminated precipitation.

641 The early ore-bearing fluids (type-A1 and A2 FI) in V2a quartz veins (Mol-II
642 mineralisation) show T_e values (-22.5°C to -33°C) consistent with a H₂O-NaCl-KCl system
643 (Hall et al., 1988), with variable amounts of other cations such as Ca²⁺, Mg²⁺. Quartz
644 geochemistry has demonstrated a hydrothermal (magmatic) origin for the mineralising
645 fluid(s) (Fig. 11). The presence of CO₂ in the type-A1 FI may thus indicate an originally low-
646 salinity and low CO₂-bearing magma-derived fluid(s). The association of low saline fluids,
647 usually containing low amounts of CO₂, is common in porphyry Mo deposits, in particular
648 within arc-related Mo deposits, such as Endako (Selby et al., 2000), Thompson Creek (e.g.,
649 Thompson Creek, Hall et al., 1984; Cannivan Gulch, Darling, 1994; Geumeum, Kim et al.,
650 2016), and, apparently, it has no effect on the size or the ore-grade of the deposit (Taylor et
651 al., 2012). Cline and Bodnar (1991, 1994) have demonstrated that when magma
652 crystallization progresses, the released fluid(s) will have less than 10% chlorine
653 concentration. Since we do not have firm evidence of fluid boiling from the FI assemblage,
654 the rare type-B, high saline (up to 32 wt.% NaCl eq.) fluids in FIs can hence be interpreted as
655 magma-sourced saline brines, segregated in the early stages of magma crystallization (Cline
656 and Bodnar, 1991; 1994). Alternatively, fluid boiling could have occurred at deeper levels,
657 predating the Mol mineralization. The vaporization of CO₂ during boiling could have
658 increased the pH, leading to precipitation of Cu from the fluids (Drummond and Ohmoto,
659 1985), whereas Mo remained dissolved in the residual fluids with lower salinity and CO₂
660 content as hydroxyl (H₂MoO₄) and alkali molybdate complexes (Ulrich and Mavrogenes,
661 2008). In addition, boiling and the associated early metal deposition could have consumed the
662 sulphur, increasing further the solubility of Mo in the residual fluids (Xiaoyun, 1989; Ulrich
663 and Mavrogenes, 2008).

664 Fluids from the phyllic alteration zone (type-A3 FI) show no evidence of CO₂ but similar
665 T_h (240-350 °C) and salinity (1.7-4.3 wt.% NaCl eq.). This is comparable with the Endako
666 porphyry Mo deposit, where the fluid chemistry associated with K-feldspar and sericite
667 alteration assemblages show no distinct differences (Selby et al., 2000). A significant
668 contribution of meteoric fluids is inferred due to the absence of CO₂ and the observed lower
669 T_h and salinities. The paragenetic occurrence of Ser (Ms) with Mol+Cb mineralisation (Mol-
670 III mineralisation) highlights the dominant role of neutralisation and cooling of acidic fluids
671 (Hemley and Hunt, 1992; Giggenbach, 1997) caused by percolating meteoric fluids and
672 mixing, which also caused the sulphide precipitation. Moreover, the coincidence of high-
673 grade Mo precipitation with very low salinity type-A4 FI could be explained by the
674 importance of hydroxyl complex (H₂MoO₄, Ulrich and Mavrogenes, 2008) for molybdenum
675 transportation (Candela and Holland, 1986) in temperatures below 300 °C (Xiaoyun, 1989).
676 Since the Mo solubility decreases with increasing salinity (Keppler and Wyllie, 1991), Mo
677 precipitation should have been facilitated by continuous fluid exsolution and mixing,
678 temperature/pressure fluctuations and/or pH changes (Audétat, 2010; Seo et al., 2012).

679 In order to better constrain the thermo-baric environment associated with Mo
680 mineralisation, FI isochores (Fig. 17a) have been constructed using the BULK and ISOC
681 softwares (Bakker, 2003). Isochores were chosen considering representative fluid inclusions
682 for type-A1 (bulk density of 0.599 g/cc) and A-4 (bulk density of 0.826 g/cc) FI. Calculations
683 were based on the equations of state of Zhang and Frantz (1987) for density and Bodnar
684 (1993), Bodnar and Vityk (1994), and Knight and Bodnar (1989) for the bulk composition.
685 The isochores are then combined with the T estimates as derived from the TitaniQ
686 thermometry for pressure correction. For the type-A1, the area in P-T space defined by the
687 intersections of isochores with T estimates is centered at 1.5 ± 0.5 kbar and $580^\circ \pm 75^\circ\text{C}$.
688 Assuming lithostatic pressure conditions, this conforms to paleogeothermal gradient of ca.
689 $100^\circ\text{C}/\text{km}$ and a depth of 7.4 km (based on a lithostatic pressure gradient of 27 MPa km^{-1})
690 for the early (V2a stage) mineralisation. This pressure/depth estimates for the mineralising
691 environment is consistent with those reported in many porphyry Mo deposits (Selby et al.,
692 2000; Taylor et al., 2012; Ni et al., 2015). This is also compatible with the marginal
693 magmatic textures (compositional layering) preserved at the roof of the main mineralised
694 body (Fig. 5a). Using the same geothermal gradient and assuming a progressive transition
695 from lithostatic to hydrostatic pressure conditions, the intersection with the type-A4 isochore
696 provides pressure estimates ranging from 0.25 (based on a hydrostatic pressure gradient of 10
697 MPa km^{-1}) to 0.75 kbar in a narrow temperature range of ca. 250 °C. These P-T estimates

698 constrain the high-grade Mo mineralisation during the V2b stage at shallower crustal levels
699 (ca. 3 km) during progressive exhumation of the mineralising system (Fig. 17a).

700 When the different FI types are plotted in a Th vs. salinity diagram, there is a
701 significant overlap in the populations of L-rich+V FI. Nonetheless, a general trend of
702 decreasing Th and salinities values from Type-A1, A2 and A3 (hosted by quartz) to type-A4
703 (hosted by paraspurite) FI can be observed (Fig. 17b). Three main groups of FI can be
704 discriminated in the Th vs. salinity diagram: (i) group-1, with the highest mean of Th, that
705 includes all the type-A1 and part of the type-A2 FI; (ii) group-2 that includes the type-A2 FI,
706 with a general trend to lower Th and salinity values; and (iii) group-3, formed by the type-A4
707 FI. Taking into consideration the fluid evolution processes typical of hydrothermal ore
708 deposits depicted in Wilkinson (2001), group-1 is consistent with isothermal mixing and
709 group-2 with meteoric fluid mixing/dilution, respectively. Group-3 is instead consistent with
710 cooling and pressurisation (Fig. 17b-c). This evidence suggests a mineralising system
711 recording the progressive evolution from a closed to an open fluid circulation system,
712 controlled by the progressive transition from a ductile to brittle environment, where rock
713 fracturing has enhanced permeability and meteoric fluids percolation and mixing.

714 **13.4. A model for the Siah Kamar Mo mineralisation**

715 Collectively, our results from the SKMD confirm a Mo mineralisation scenario
716 compatible with an Endako-type porphyry Mo deposit (see also Nabatian et al., 2017b).
717 Nonetheless, our results also point to peculiar characteristics for the SKMD. The main
718 peculiarity of the SKMD is a prolonged history of magma production and emplacement (ca.
719 4-5 Ma). In fact, despite that multiple magma intrusion processes are common in the
720 evolution of porphyry systems, the time lapse from early- to late-stage mineralisation is
721 usually less than 1 m.y. (Sillitoe, 2010; Mercer et al., 2015). Therefore the SKMD can be
722 classified as an uncommon porphyry Mo mineralization, which operated in a time scale of at
723 least 4-5 Ma. Such mineralisation time scales have been reported from giant and large
724 porphyry systems (e.g., Chuquicamata, Correa et al., 2016; and Halasu, Xue et al., 2016).

725 The concurrence of carbonatization and Mo mineralisation is also a peculiar
726 characteristic of the SKMD. Carbonate precipitation is uncommon in porphyry systems
727 (Taylor et al., 2012) and carbonate veins commonly, which occurred in the latest stages, are
728 either barren (e.g., Selby et al., 2000; Seedorff and Einaudi, 2004; Mao et al., 2011; Ni et al.,
729 2015) or with only minor Mo enrichment (e.g., Yang, 2007; Wang et al., 2017; Zhai et al.,
730 2017).

731 Therefore, any model for the formation of the Mo Siah Kamar mineralisation should take
732 into consideration the following constraints: (i) the U-Pb zircon magmatic ages and the Rb-Sr
733 ages of the alteration mineralogy support a two-stage mineralisation process: early (at ca. 33
734 Ma) low-grade disseminated mineralization (stage-I, Mol-I) during potassic-sodic alteration
735 in a reducing environment and subsequent (at ca 28-29 Ma) high-grade stockwork Mo
736 mineralisation (stage-II, Mol-II and Mol-III, as constrained by the Re-Os Mol
737 geochronology) during phyllic alteration; (ii) the two-stage mineralisation is associated with
738 multiphase intrusions and transition from basic to acidic magmatism, in a time lapse of ca. 4-
739 5 Ma; (iii) the mineralising fluid(s) records transition from a magmatic/hydrothermal- to a
740 meteoric-dominated system across a progressive ductile-to-brittle environment (temperature
741 range from ~600 to 250 °C); and (iv) the dominant role of carbonate precipitation and
742 neutralisation of acidic fluids in the Mo mineralisation (Mol+Ser+Cb assemblage) during
743 fluid cooling.

744 Based on the synchronicity (in the time lapse 28-29 Ma) existing between the
745 crystallisation of the acidic dyke and stock at the rims of the mineralised zone (Fig. 3),
746 phyllic alteration and Mo-mineralisation, it is postulated that mineralising fluids were sourced
747 from these acidic intrusives. Nonetheless, these acidic magmatic rocks are Mo-barren. We
748 then propose a model of Mo mineralisation as primarily caused by the re-fertilisation (ore
749 enhancement) induced by the renewed magma supply at 28-29 Ma. The exposed acidic
750 intrusions are considered as the apophyses of a magmatic system likely supported by a
751 voluminous magma chamber at depth, able to sustain highly perturbed geothermal conditions
752 and renewed fluid supply within the early formed potassic-sodic alteration zone formed at ca.
753 33 Ma (Fig. 18). In such a scenario, the mode of fluid exsolution was controlled and
754 modulated by the rheological evolution of the solidifying shell surrounding the cooling
755 magma. At high-temperature conditions ($T > 600$ °C), fluid-rock equilibrium was likely
756 attained and fluids were entrapped in solidifying magma at depth (ca. 7 km). When
757 temperature decreased and brittle deformation prevailed, more fluids were released into the
758 system and interacted with the ground waters (e.g., Giggenbach, 1997). At this stage ($T <$
759 300 °C), the CO_2 dissolved in the fluids became reactive and the release of CO_2 caused
760 acidification of the fluids (Giggenbach and Soto, 1992; Kaszuba et al., 2005; Little and
761 Jackson, 2010) and significant interaction with the country rocks, leading to mineral
762 dissolution and metal leaching (Bandstra and Brantley, 2008; Liu et al., 2012; Kirsch et al.,
763 2014; Lions et al., 2014) from the early-formed potassic-sodic alteration zone. The deposition
764 zone is thus interpreted as zone of fluid mixing with meteoric ground water, when fluid

765 neutralization and temperature drop down leading to the Ms-Cb precipitation and metal (Mol)
766 mineralisation in the system, focused by structurally-controlled pathways assisted by
767 continuous fracturing of the intrusive carapace.

768

769 **13.5. Correlation at regional scale**

770 Similar Eocene-Oligocene high-K calc-alkaline to shoshonitic magmatism as reported
771 from the SKMD (Khaleghi et al., 2013; Nabatian et al., 2017b) has been also reported in
772 many studies along the UDMZ, AMZ, BAMZ, Lesser Caucasus, and the western Alborz
773 (e.g., Aftabi and Atapour, 2000; Ahmadian et al., 2009; Aghazadeh et al., 2010; Sarjoughian
774 et al., 2012; Kananian et al., 2014; Jamali and Mehrabi, 2015) (Fig. 1). Within this context,
775 the SKMD shows the oldest reported ages among the porphyry deposits within the UDMZ
776 (except the Kal-e-Kafi porphyry Cu-Mo deposit, with zircon U-Pb age of 52-50 Ma,
777 Ahmadian et al., 2016), and only two porphyry Cu-Mo-Au deposits have been reported
778 within the same time window including Bondar-e-Hanza (with Mol Re-Os age of 28.4 ± 0.5
779 Ma, Aghazadeh et al., 2015) and Reagan (with zircon U-Pb age of 29.3 ± 0.2 Ma,
780 Hassanzadeh, 1993) (Fig. 1 and supplementary material #1).

781 By contrast, many porphyry Cu-Mo deposits with older (Eocene) and similar (Oligocene)
782 ages have been reported in the AMZ (Haftcheshmeh Cu-Mo, Mol Re-Os age of 28.2-27.1
783 Ma, Aghazadeh et al., 2015) and Lesser Caucasian magmatic zones (Kadjaran Cu-Mo; 27.3–
784 26.4 Ma, Rezeau et al., 2016). Nonetheless, apart from the SKMD, none of these porphyry
785 systems shows Mo as the first commodity. In particular, whereas the Mo/Cu ratio within
786 SKMD is about 1, the coeval porphyry Cu-Mo deposits of Kadjaran, Haftcheshmeh, and Kal-
787 e Kafi show values of about 0.1, which are significantly higher than the Miocene ones
788 (supplementary material #1). The Mo enrichment in the Eocene-Oligocene porphyry systems
789 could be attributed to either to a relatively deeper emplacement level of the metal-bearing
790 magma (Candela, 1986) or to the contribution and re-fertilisation of a preexisting Mo-
791 enriched crustal source (Farmer and DePaolo, 1984; Wan et al., 2018).

792

793 **14. Conclusions**

794 The main results of this study can be summarised as follows:

795 (1) The SKMD developed during a long-lived magmatic and alteration history, spanning
796 from ca. 33 Ma to 29-28 Ma, associated with a diachronous, low- and high-grade Mo
797 mineralisation.

798 (2) Re-fertilisation of an early formed disseminated Mo ore by renewed magmatism and
799 associated magma degassing and fluid exsolution is proposed as the scenario for ore
800 enhancement and, consequently, for high-grade Mo mineralisation.

801 (3) Leaching of metals from the early formed disseminated ore bodies operated by acidic
802 fluids exsolved from the cooling magmas is recognised as the cause of Mo-enrichment in the
803 mineralising fluids.

804 (4) Mixing of magmatic and meteoric fluids during progressive embrittlement (and cooling)
805 of the mineralising environment is considered as the key factor leading to the high-grade Mo
806 ore formation, through progressive neutralisation of the acidic fluids via structurally-
807 controlled carbonation and sericitisation.

808 Comparison at a regional scale indicates that parameters such as longevity of magma
809 supply, progressive magma crystallization/differentiation and the presence of a possible pre-
810 enriched crustal material should be considered for the Mo endowment in the UMDZ.

811

812 **Acknowledgements**

813 This research is part of the first Author PhD program at the Roma Tre University. The Grant
814 to Department of Science, Roma Tre University (MIUR-Italy Dipartimenti di Eccellenza,
815 ARTICOLO 1, COMMI 314 – 337 LEGGE 232/2016) is gratefully acknowledged. DS –
816 Total Endowment Fund, CUG Dida Scholarship, Antonia Hofmann, Chros Ottley, Geoff
817 Nowell. We are indebted to K. Yamamoto for support and providing access to the XRF, ICP-
818 MS and LA-ICP-MS facilities at Nagoya University. We thank T. Theye for advice and for
819 granting access to electron microprobe and LA-ICP-MS facilities at the Institut für
820 Mineralogie und Kristallchemie at the University of Stuttgart. We also thank C. Romano for
821 granting access to the Raman Spectroscopy facility at the Department of Science, Roma Tre
822 University. We thank the Aria Kansar Samin Co for sharing their data on the Siah-Kamar Mo
823 deposit and for granting access to the mineralisation area. This manuscript benefitted of
824 constructive comments and advice from D. Lentz and an anonymous reviewer. We also thank
825 the editorial handling by F. Pirajno.

827

828 **APPENDIX:**829 **Analytical techniques**830 **LA-ICP-MS quartz trace element geochemistry**

831 Based on petrographic observations (optical and BSE) and mineral chemistry on polished
832 thin-section samples, 16 representative quartz crystals were selected for in situ trace and
833 REEs element analyses, using laser ablation (LA, CETAC LSX-213 laser system) combined
834 with an inductively coupled plasma mass spectrometer (ICP-MS, AGILENT 7700) at Institut
835 für Mineralogie, Universität Stuttgart. The following laser ablation parameters were used:
836 spot diameter 50 μm , 60% laser power (100% = 4 mJ at a spot diameter of 150 μm), 10 Hz
837 laser pulse repetition rate, and a mixed helium and argon gas flow with 500 ml/min and 800
838 ml/min, respectively, serving as carrier of the ablated material.

839 The data acquisition was performed using the Agilent Mass Hunter software (version
840 B.01.01). Each analysis comprised the acquisition of the individual background ion
841 intensities (gas-blank) for roughly 23 s followed by the acquisition of the ion intensities on
842 laser irradiation of the sample spot for roughly 57 s.

843 The method involved monitoring of 18 isotopes (^7Li , ^9Be , ^{11}B , ^{27}Al , $^{28,29}\text{Si}$, ^{31}P , ^{44}Ca ,
844 $^{47,49}\text{Ti}$, ^{55}Mn , $^{56,57}\text{Fe}$, ^{71}Ga , $^{72,73}\text{Ge}$, ^{75}As , ^{85}Rb , ^{88}Sr ; this selection excludes isobaric
845 interferences of isotopes from other elements) using individual integration times of 10 ms.

846 Reference materials were DLH7 and DLH8 glasses from P&H Developments Ltd., and
847 NIST (National Institute of Standards and Technology, USA) 612 and 610 glasses. Certified,
848 recommended and proposed values for these reference materials are from Jochum et al.

849 (2011). The validity of the calibration, data evaluation, and reproducibility were checked
850 with the reference materials Diorite (DRN) and Zinnwaldite (ZW-C) from Service
851 d'Analyses des Roches et des Minéraux du CNRS. Lithium-borate glass disks of both were
852 prepared using 0.6 g of powder of these reference materials and 3.6 g of lithium borate. All
853 elemental concentrations were calculated relative to the silicon elemental concentration as
854 internal standard which was determined from the results of the ^{29}Si isotope. The absolute
855 silicon concentration was previously measured with the EMP. The same spot target was
856 applied for both EMP and LA-ICP-MS. Precision is estimated better than 5%. The software
857 used for calibration and data evaluation was developed by J. Opitz (Massonne et al., 2013;
858 Baggio et al., 2018).

859

860 **Fluid inclusion microthermometry**

861 Samples representative of the different mineralised quartz-carbonate vein sets were prepared
862 as 150- μm -thick doubly polished wafers and petrography studies were carried out with a
863 polarizing microscope to define the types of fluid inclusions, the populations and their
864 genetic relationships. Microthermometric measurements were made utilizing a Linkam
865 THMSG600 freezing– heating stage at the Istituto di Geologia Ambientale e Geoingegneria
866 of CNR at the University of Roma “La Sapienza”. The systems were calibrated using pure
867 natural CO_2 inclusions for low temperatures and synthetic pure water fluid inclusions for
868 high temperatures, respectively. Reproducibility of the triple point of CO_2 at $-56.6\text{ }^\circ\text{C}$ and
869 pure H_2O critical point at $374\text{ }^\circ\text{C}$ were $\pm 0.3\text{ }^\circ\text{C}$ and $\pm 0.5\text{ }^\circ\text{C}$ respectively. Low temperature
870 (T_e , T_m) data were determined with a $1\text{--}5\text{ }^\circ\text{C}/\text{min}$ rate, whereas high temperature (T_h , T_{ms})
871 data with a heating rate of $5\text{--}20\text{ }^\circ\text{C}/\text{min}$, respectively. Bulk composition and Isochores for
872 various FI types were calculated by BULK and ISOC softwares provided by (Bakker, 2003).

873 **Raman spectroscopy**

874 A HORIBA LabRAM HR Raman spectrometer at the Dipartimento di Scienze, Università
875 degli Studi di Roma Tre, calibrated using a silicon standard, was employed to acquire the
876 Raman spectra. The micro-Raman spectrometer is equipped with a green argon ion laser (532
877 nm), focused through a $50\times$ and $100\times$ objectives. Optical filters were employed in order to
878 achieve $\sim 2.5\text{ mW}$ at the surface of the glassy interface. The Raman systems were set with 600
879 T and 1200 T gratings, exposure time 20 s (3 times), confocal hole of $200\text{--}500\text{ }\mu\text{m}$, and slit of
880 $200\text{ }\mu\text{m}$, and the spatial resolution of the sample surface is $\sim 1\text{ }\mu\text{m}$ (theoretical spatial
881 resolution = $0.61\lambda/\text{NA}$ where λ is the wavelength of the laser (532 nm), and NA is the
882 numerical aperture of the microscope objective being used (0.9 for $100\times$). Raman spectra
883 were acquired over the range from 90 to 2000 cm^{-1} . Reference values from Frezzotti et al.
884 (2012) for common gases inside fluid inclusions and some minerals were used to interpret the
885 obtained spectra. Furthermore, the CrystalSleuth software (<http://rruff.info/>) was employed to
886 define the accessory minerals.

887 **Zircon U-Pb Geochronology**

888 The zircon U-Pb geochronology study was carried out at the Department of Earth and
889 Environmental Sciences of Nagoya University. Four samples were selected for zircon grains
890 separation. More than 10 kg for each sample were collected and crushed. Only few zircon
891 grains (ca. 30) were found. Some of them were useless due to the small grain size ($< 30\text{ }\mu\text{m}$)
892 or to the strongly fractured crystal structure. Cathodoluminescence (CL) and Back Scatter

893 (BSE) imaging was used first to gather information on the grain texture and internal growth
894 and/or alteration zoning. Zircon grains with intense fracturing and inclusions were avoided.
895 The zircon grains were analyzed by LA-ICP-MS (Agilent 7700XICPMS machine connected
896 with NWR213 (Electro Scientific Industries) laser ablation system (Kouchi et al., 2015). A
897 standard glass (NIST SRM 610) and two zircon standards, named 91500 (1059 Ma,
898 Wiedenbeck et al., 1995) and OD-3 (33.1 Ma, Iwano et al., 2013) were used. Blanks, the
899 zircon standards, and the standard glass were measured at the beginning and ending of each
900 measurement cycle. Eight points were measured in each cycle. The ISOPLOT V4.15
901 software (Ludwig, 2011) was utilized to calculate the Concordia, statistics and to prepare the
902 age plots. Correction for the common Pb was performed using ^{204}Pb intensity (Cox and
903 Wilton, 2006). Most of the results with high common Pb (values more than 20 %) were
904 excluded from calculations.

905 **Molybdenite Re-Os geochronology**

906 Molybdenite grains were isolated from samples and then gently were milled, washed and
907 dried (Selby and Creaser, 2004). Impurities were separated under microscope and about 100
908 mg of pure molybdenite was prepared for each sample with the analytical protocol following
909 that of (Selby and Creaser, 2004). The Re-Os molybdenite analysis were performed in the
910 Laboratory for Sulfide and Source Rock Geochronology and Geochemistry and the Arthur
911 Holmes Laboratory in the Durham Geochemistry Centre at Durham University (UK). In
912 brief, molybdenite samples were dissolved and equilibrated with a known amount of ^{185}Re
913 and isotopically normal Os in inverse aqua regia (2:1 16 N HNO_3 and 12 N HCl , 3 mL) at
914 240 °C for 24 h in a Carius-tube. Rhenium and Os were isolated and purified by solvent
915 extraction, microdistillation, and anion exchange chromatography, and analyzed by negative
916 thermal ionization mass spectrometry on a ThermoScientific TRITON mass spectrometer
917 using Faraday collectors. Total procedural blanks for Re and Os 2.5 pg and 0.1 pg,
918 respectively, with an Os blank composition of 0.21 0.02 (n 6), which are insignificant to the
919 Re and Os levels in the analysed samples. Rhenium and Os concentrations, and Re-Os
920 molybdenite date uncertainties are presented at the 2σ level, which includes the uncertainties
921 in Re and Os mass spectrometer measurement, spike and standard Re and Os isotopic
922 compositions, and calibration uncertainties. Because a mixed tracer solution is used,
923 uncertainties in weights of sample and tracer solution do not affect the calculated age, and are
924 not considered. However, sample and tracer solution weight uncertainties are considered in

925 determining the uncertainty in the Re and ^{187}Os concentrations. Uncertainty in the ^{187}Re
926 decay constant (0.35%, Smoliar et al., 1996) is also considered.

927

928 **Rb-Sr multiminerall geochronology**

929 To determine the ages of mineral assemblage crystallization, we employed the Rb-Sr
930 internal mineral isochron approach. Age information mainly is based on the high-Rb/Sr
931 phases muscovite/sericite, and biotite. Mineral separates were prepared following Glodny et
932 al. (2008). Crushing was performed by hand using pestle and mortar combined with repeated
933 sieving, to preserve the original grain sizes of minerals. Rb–Sr isotopic data were acquired at
934 GFZ Potsdam using a Thermo Scientific TRITON thermal ionization mass spectrometer. Sr
935 isotopic compositions were measured in dynamic multi-collection mode. Rb isotope dilution
936 analysis was done in static multi-collection mode. The value obtained for $^{87}\text{Sr}/^{86}\text{Sr}$ of the
937 NIST SRM 987 reference material was 0.710255 ± 0.000024 (2σ , $n = 23$). For age
938 calculation, uncertainties of $\pm 0.005\%$ for $^{87}\text{Sr}/^{86}\text{Sr}$ and of $\pm 1.5\%$ for $^{87}\text{Rb}/^{86}\text{Sr}$ ratios were
939 assigned to the results. Uncertainties of isotope and age data are quoted at 2σ . The program
940 ISOPLOT/EX 4.15 (Ludwig, 2011) was used for calculating regression lines. Decay
941 constants are those recommended by Villa et al. (2015).

942

944 **References**

- 945 Aftabi, A., Atapour, H., 2000. Regional aspects of shoshonitic volcanism in Iran.
946 Episodes 23, 119-125.
- 947 Aghanabati, A., 2004. Geology of Iran, GSI Publication, Tehran.
- 948 Aghazadeh, M., Castro, A., Omran, N.R., Emami, M.H., Moinvaziri, H., Badrzadeh, Z.,
949 2010. The gabbro (shoshonitic)–monzonite–granodiorite association of Khankandi
950 pluton, Alborz Mountains, NW Iran. *Journal of Asian Earth Sciences* 38, 199-219.
- 951 Aghazadeh, M., Hou, Z., Badrzadeh, Z., Zhou, L., 2015. Temporal–spatial distribution
952 and tectonic setting of porphyry copper deposits in Iran: Constraints from zircon U–Pb
953 and molybdenite Re–Os geochronology. *Ore Geology Reviews* 70, 385-406.
- 954 Ahmadian, J., Haschke, M., McDonald, I., Regelous, M., RezaGhorbani, M., Emami,
955 M.H., Murata, M., 2009. High magmatic flux during Alpine-Himalayan collision:
956 Constraints from the Kal-e-Kafi complex, central Iran. *Geological Society of America*
957 *Bulletin* 121, 857-868.
- 958 Ahmadian, J., Sarjoughian, F., Lentz, D., Esna-Ashari, A., Murata, M., Ozawa, H., 2016.
959 Eocene K-rich adakitic rocks in the Central Iran: implications for evaluating its Cu–Au–
960 Mo metallogenic potential. *Ore Geology Reviews* 72, 323-342.
- 961 Amidi, M., Alavi Tehrani, M., Lotfi, P., Haghypour, A., Sabzehei, M., Behroozi, A.,
962 Lescuyer, J., Riou, R., 1987. Geological map of Mianeh. Geological Survey of Iran,
963 Tehran.
- 964 Aria Kansar Samin Co., u.r., 2013. Report on exploratory operations of Siah-Kamar
965 molybdenum occurrence.
- 966 Asadi, S., Moore, F., Zarasvandi, A., 2014. Discriminating productive and barren
967 porphyry copper deposits in the southeastern part of the central Iranian volcano-plutonic
968 belt, Kerman region, Iran: a review. *Earth-Science Reviews* 138, 25-46.
- 969 Audétat, A., 2010. Source and evolution of molybdenum in the porphyry Mo (–Nb)
970 deposit at Cave Peak, Texas. *Journal of Petrology* 51, 1739-1760.
- 971 Audetat, A., Pettke, T., Heinrich, C., Bodnar, R., 2008. The composition of magmatic-
972 hydrothermal fluids in barren and mineralized intrusions: *economic geology*, v. 103.
- 973 Ayati, F., Yavuz, F., Asadi, H.H., Richards, J.P., Jourdan, F., 2013. Petrology and
974 geochemistry of calc-alkaline volcanic and subvolcanic rocks, Dalli porphyry copper–
975 gold deposit, Markazi Province, Iran. *International Geology Review* 55, 158-184.
- 976 Ayres, L., Averill, S., Wolfe, W., 1982. An Archean molybdenite occurrence of possible
977 porphyry type at Setting Net Lake, northwestern Ontario, Canada. *Economic Geology* 77,
978 1105-1119.
- 979 Babazadeh, S., Ghorbani, M.R., Bröcker, M., D'Antonio, M., Cottle, J., Gebbing, T.,
980 Carmine Mazzeo, F., Ahmadi, P., 2017. Late Oligocene–Miocene mantle upwelling and
981 interaction inferred from mantle signatures in gabbroic to granitic rocks from the
982 Urumieh–Dokhtar arc, south Ardestan, Iran. *International Geology Review* 59, 1590-
983 1608.
- 984 Baggio, S.B., Hartmann, L.A., Lazarov, M., Massonne, H.-J., Opitz, J., Theye, T.,
985 Viefhaus, T., 2018. Origin of native copper in the Paraná volcanic province, Brazil,

- 986 integrating Cu stable isotopes in a multi-analytical approach. *Mineralium Deposita* 53,
987 417-434.
- 988 Bakker, R.J., 2003. Package FLUIDS 1. Computer programs for analysis of fluid
989 inclusion data and for modelling bulk fluid properties. *Chemical Geology* 194, 3-23.
- 990 Ballato, P., Cifelli, F., Heidarzadeh, G., Ghassemi, M.R., Wickert, A.D., Hassanzadeh, J.,
991 Dupont-Nivet, G., Balling, P., Sudo, M., Zeilinger, G., Schmitt, A.K., Mattei, M.,
992 Strecker, M.R., 2017a. Tectono-sedimentary evolution of the northern Iranian Plateau:
993 insights from middle-late Miocene foreland-basin deposits. *Basin Research* 29, 417-446.
- 994 Ballato, P., Cifelli, F., Heidarzadeh, G., Ghassemi, M.R., Wickert, A.D., Hassanzadeh, J.,
995 Dupont - Nivet, G., Balling, P., Sudo, M., Zeilinger, G., 2017b. Tectono - sedimentary
996 evolution of the northern Iranian Plateau: insights from middle-late Miocene
997 foreland - basin deposits. *Basin Research* 29, 417-446.
- 998 Bandstra, J.Z., Brantley, S.L., 2008. Surface evolution of dissolving minerals
999 investigated with a kinetic Ising model. *Geochimica et Cosmochimica Acta* 72, 2587-
1000 2600.
- 1001 Berberian, M., King, G., 1981. Towards a paleogeography and tectonic evolution of Iran.
1002 *Canadian Journal of Earth Sciences* 18, 210-265.
- 1003 Berzina, A., Berzina, A., Gimon, V., Bayanova, T., Kiseleva, V.Y., Krymskii, R.S.,
1004 Lepekhina, E., Paleskii, S., 2015. The Zhireken porphyry Mo ore-magmatic system
1005 (eastern Transbaikalia): U-Pb age, sources, and geodynamic setting. *Russian Geology*
1006 and *Geophysics* 56, 446-465.
- 1007 Berzina, A.N., Sotnikov, V.I., Economou-Eliopoulos, M., Eliopoulos, D.G., 2005.
1008 Distribution of rhenium in molybdenite from porphyry Cu-Mo and Mo-Cu deposits of
1009 Russia (Siberia) and Mongolia. *Ore Geology Reviews* 26, 91-113.
- 1010 Blevin, P.L., Chappell, B.W., 1992. The role of magma sources, oxidation states and
1011 fractionation in determining the granite metallogeny of eastern Australia. *Earth and*
1012 *Environmental Science Transactions of The Royal Society of Edinburgh* 83, 305-316.
- 1013 Bloom, M.S., 1981. Chemistry of inclusion fluids; stockwork molybdenum deposits from
1014 Questa, New Mexico, Hudson Bay Mountain and Endako, British Columbia. *Economic*
1015 *Geology* 76, 1906-1920.
- 1016 Bodnar, R., 1993. Revised equation and table for determining the freezing point
1017 depression of H₂O-NaCl solutions. *Geochimica et Cosmochimica Acta* 57, 683-684.
- 1018 Bodnar, R., Vityk, R., 1994. Interpretation of microthermometric data for H₂O-NaCl
1019 fluid inclusions. *Fluid inclusions in minerals: Methods and applications. . Short course of*
1020 *the working group, Inclusions in Minerals*, 117-130.
- 1021 Candela, P.A., 1992. Controls on ore metal ratios in granite-related ore systems: an
1022 experimental and computational approach. *Earth and Environmental Science*
1023 *Transactions of The Royal Society of Edinburgh* 83, 317-326.
- 1024 Candela, P.A., Holland, H.D., 1986. A mass transfer model for copper and molybdenum
1025 in magmatic hydrothermal systems; the origin of porphyry-type ore deposits. *Economic*
1026 *Geology* 81, 1-19.
- 1027 Caputo, R., 1995. Evolution of orthogonal sets of coeval extension joints. *Terra Nova* 7,
1028 479-490.

- 1029 Castro, A., Aghazadeh, M., Badrzadeh, Z., Chichorro, M., 2013. Late Eocene–Oligocene
1030 post-collisional monzonitic intrusions from the Alborz magmatic belt, NW Iran. An
1031 example of monzonite magma generation from a metasomatized mantle source. *Lithos*
1032 180-181, 109-127.
- 1033 Cathles, L.M., Erendi, A., Barrie, T., 1997. How long can a hydrothermal system be
1034 sustained by a single intrusive event? *Economic Geology* 92, 766-771.
- 1035 Chiaradia, M., Merino, D., Spikings, R., 2009. Rapid transition to long-lived deep crustal
1036 magmatic maturation and the formation of giant porphyry-related mineralization
1037 (Yanacocha, Peru). *Earth and Planetary Science Letters* 288, 505-515.
- 1038 Chiu, H.-Y., Chung, S.-L., Zarrinkoub, M.H., Mohammadi, S.S., Khatib, M.M., Iizuka,
1039 Y., 2013. Zircon U–Pb age constraints from Iran on the magmatic evolution related to
1040 Neotethyan subduction and Zagros orogeny. *Lithos* 162, 70-87.
- 1041 Cline, J.S., Bodnar, R.J., 1991. Can economic porphyry copper mineralization be
1042 generated by a typical calc - alkaline melt? *Journal of Geophysical Research: Solid Earth*
1043 96, 8113-8126.
- 1044 Cline, J.S., Bodnar, R.J., 1994. Direct evolution of brine from a crystallizing silicic melt
1045 at the Questa, New Mexico, molybdenum deposit. *Economic Geology* 89, 1780-1802.
- 1046 Colville, A.A., Colville, P.A., 1977. Paraspurrite, a new polymorph of spurrite from Inyo
1047 County, California. *American Mineralogist* 62, 1003-1005.
- 1048 Corfu, F., Hanchar, J.M., Hoskin, P.W.O., Kinny, P., 2003. Atlas of Zircon Textures.
1049 *Reviews in Mineralogy and Geochemistry* 53, 469-500.
- 1050 Correa, K.J., Rabbia, O.M., Hernández, L.B., Selby, D., Astengo, M., 2016. The timing
1051 of magmatism and ore formation in the El Abra porphyry copper deposit, northern Chile:
1052 Implications for long-lived multiple-event magmatic-hydrothermal porphyry systems.
1053 *Economic Geology* 111, 1-28.
- 1054 Cox, R.A., Wilton, D.H., 2006. U–Pb dating of perovskite by LA-ICP-MS: an example
1055 from the Oka carbonatite, Quebec, Canada. *Chemical Geology* 235, 21-32.
- 1056 Darling, R.S., 1994. Fluid inclusion and phase equilibrium studies at the Cannivan Gulch
1057 molybdenum deposit, Montana, USA: Effect of CO₂ on molybdenite-powellite stability.
1058 *Geochimica et Cosmochimica Acta* 58, 749-760.
- 1059 Dennen, W., 1966. Stoichiometric substitution in natural quartz. *Geochimica et*
1060 *Cosmochimica Acta* 30, 1235-1241.
- 1061 Doebrich, J.L., Garside, L.J., Shawe, D.R., 1996. Characterization of mineral deposits in
1062 rocks of the Triassic to Jurassic magmatic arc of western Nevada and eastern California.
1063 Citeseer.
- 1064 Drummond, S., Ohmoto, H., 1985. Chemical evolution and mineral deposition in boiling
1065 hydrothermal systems. *Economic Geology* 80, 126-147.
- 1066 Duke, C.P., 2007. Pidgeon Molybdenum project: Toronto, Ontario, Wardrop Engineering
1067 Inc., NI 34–101 Compliant Report for MPH Ventures Corporation. 92.
- 1068 Farmer, G.L., DePaolo, D.J., 1984. Origin of Mesozoic and Tertiary granite in the
1069 western United States and implications for Pre-Mesozoic crustal structure: 2. Nd and Sr
1070 isotopic studies of unmineralized and Cu- and Mo-mineralized granite in the Precambrian
1071 Craton. *Journal of Geophysical Research: Solid Earth* 89, 10141-10160.

- 1072 Fazel, E.T., Mehrabi, B., Shabani, A.A.T., 2015. Kuh-e Dom Fe–Cu–Au prospect,
1073 Anarak metallogenic complex, Central Iran: a geological, mineralogical and fluid
1074 inclusion study. *Mineralogy and Petrology* 109, 115-141.
- 1075 Frezzotti, M.L., Tecce, F., Casagli, A., 2012. Raman spectroscopy for fluid inclusion
1076 analysis. *Journal of Geochemical Exploration* 112, 1-20.
- 1077 Giggenbach, W., 1997. The origin and evolution of fluids in magmatic-hydrothermal
1078 systems. *Geochemistry of hydrothermal ore deposits*.
- 1079 Giggenbach, W.F., Soto, R.C., 1992. Isotopic and chemical composition of water and
1080 steam discharges from volcanic-magmatic-hydrothermal systems of the Guanacaste
1081 Geothermal Province, Costa Rica. *Applied Geochemistry* 7, 309-332.
- 1082 Glazner, A.F., Bartley, J.M., Coleman, D.S., Gray, W., Taylor, R.Z., 2004. Are plutons
1083 assembled over millions of years by amalgamation from small magma chambers? *GSA*
1084 *today* 14, 4-12.
- 1085 Glodny, J., Kühn, A., Austrheim, H., 2008. Geochronology of fluid-induced eclogite and
1086 amphibolite facies metamorphic reactions in a subduction–collision system, Bergen Arcs,
1087 Norway. *Contributions to Mineralogy and Petrology* 156, 27-48.
- 1088 Hall, D.L., Sterner, S.M., Bodnar, R.J., 1988. Freezing point depression of NaCl-KCl-H
1089 2O solutions. *Economic Geology* 83, 197-202.
- 1090 Hall, W., Schmidt, E., Howe, S., Broch, M., 1984. The Thompson Creek, Idaho,
1091 porphyry molybdenum deposit—an example of a fluorine-deficient molybdenum
1092 granodiorite system, International Association on the Genesis of Ore Deposits 6th
1093 Symposium, Tbilisi 1982, Proceedings, pp. 349-357.
- 1094 Haschke, M., Ahmadian, J., Murata, M., McDonald, I., 2010. Copper Mineralization
1095 Prevented by Arc-Root Delamination during Alpine-Himalayan Collision in Central Iran.
1096 *Economic Geology* 105, 855-865.
- 1097 Hassanpour, S., Alirezaei, S., Selby, D., Sergeev, S., 2014. SHRIMP zircon U–Pb and
1098 biotite and hornblende Ar–Ar geochronology of Sungun, Haftcheshmeh, Kighal, and
1099 Niaz porphyry Cu–Mo systems: evidence for an early Miocene porphyry-style
1100 mineralization in northwest Iran. *International Journal of Earth Sciences* 104, 45-59.
- 1101 Hassanzadeh, J., 1993. Metallogenic and tectono-magmatic events in the SE sector of the
1102 Cenozoic active continental margin of Iran (Shahr-e-Babak area, Kerman province). (Ph.
1103 D. Thesis). University of California.
- 1104 Hassanzadeh, J., Stockli, D.F., Horton, B.K., Axen, G.J., Stockli, L.D., Grove, M.,
1105 Schmitt, A.K., Walker, J.D., 2008. U-Pb zircon geochronology of late Neoproterozoic–
1106 Early Cambrian granitoids in Iran: Implications for paleogeography, magmatism, and
1107 exhumation history of Iranian basement. *Tectonophysics* 451, 71-96.
- 1108 Hawkesworth, C., Blake, S., Evans, P., Hughes, R., Macdonald, R., Thomas, L., Turner,
1109 S., Zellmer, G., 2000. Time scales of crystal fractionation in magma chambers—
1110 integrating physical, isotopic and geochemical perspectives. *Journal of Petrology* 41,
1111 991-1006.
- 1112 Heidari, S.M., Daliran, F., Paquette, J.-L., Gasquet, D., 2015. Geology, timing, and
1113 genesis of the high sulfidation Au (–Cu) deposit of Touzlar, NW Iran. *Ore Geology*
1114 *Reviews* 65, 460-486.

- 1115 Heidarzadeh, G., Ballato, P., Hassanzadeh, J., Ghassemi, M.R., Strecker, M.R., 2017.
1116 Lake overflow and onset of fluvial incision in the Iranian Plateau: Insights from the
1117 Mianeh Basin. *Earth and Planetary Science Letters* 469, 135-147.
- 1118 Heinhorst, J., Lehmann, B., Ermolov, P., Serykh, V., Zhurutin, S., 2000. Paleozoic
1119 crustal growth and metallogeny of Central Asia: evidence from magmatic-hydrothermal
1120 ore systems of Central Kazakhstan. *Tectonophysics* 328, 69-87.
- 1121 Hemley, J., Hunt, J., 1992. Hydrothermal ore-forming processes in the light of studies in
1122 rock-buffered systems; II, Some general geologic applications. *Economic Geology* 87,
1123 23-43.
- 1124 Hosseini, M.R., Hassanzadeh, J., Alirezaei, S., Sun, W., Li, C.-Y., 2017. Age revision of
1125 the Neotethyan arc migration into the southeast Urumieh-Dokhtar belt of Iran:
1126 Geochemistry and U–Pb zircon geochronology. *Lithos* 284-285, 296-309.
- 1127 Huang, R., Audétat, A., 2012. The titanium-in-quartz (TitaniQ) thermobarometer: A
1128 critical examination and re-calibration. *Geochimica et Cosmochimica Acta* 84, 75-89.
- 1129 Huber, H., 1977. Geological map of Iran at scale of 1: 1,000,000, National Iranian Oil
1130 Co., Tehran, Iran.
- 1131 Innocenti, F., Mazzuoli, R., Pasquare, G., Radicati di Brozolo, F., Villari, L., 1982.
1132 Tertiary and quaternary volcanism of the Erzurumkars area (Eastern Turkey):
1133 geochronological data and geodynamic evolution. *Journal of Volcanology and*
1134 *Geothermal Research* 13, 223-240.
- 1135 Ishihara, S., 1988. Rhenium contents of molybdenites in granitoid-series rocks in Japan.
1136 *Economic Geology* 83, 1047-1051.
- 1137 Iwano, H., Orihashi, Y., Hirata, T., Ogasawara, M., Danhara, T., Horie, K., Hasebe, N.,
1138 Sueoka, S., Tamura, A., Hayasaka, Y., 2013. An inter - laboratory evaluation of OD - 3
1139 zircon for use as a secondary U–Pb dating standard. *Island Arc* 22, 382-394.
- 1140 Jamali, H., Mehrabi, B., 2015. Relationships between arc maturity and Cu–Mo–Au
1141 porphyry and related epithermal mineralization at the Cenozoic Arasbaran magmatic belt.
1142 *Ore Geology Reviews* 65, 487-501.
- 1143 Janković, S., 1982. Yugoslavia, in Dunning, F.W., Mykura, W., and Slater, D., eds.,
1144 *Mineral deposits of Europe, v. 2, Southeast Europe: Institution of Mining and*
1145 *Metallurgy* Mineralogical Society, London, p. 143–202.
- 1146 Jochum, K.P., Weis, U., Stoll, B., Kuzmin, D., Yang, Q., Raczek, I., Jacob, D.E., Stracke,
1147 A., Birbaum, K., Frick, D.A., 2011. Determination of reference values for NIST SRM
1148 610–617 glasses following ISO guidelines. *Geostandards and Geoanalytical Research* 35,
1149 397-429.
- 1150 John, D., Ayuso, R., Barton, M., Blakely, R., Bodnar, R., Dilles, J., Gray, F., Graybeal,
1151 F., Mars, J., McPhee, D., 2010. Porphyry copper deposit model, chap. B of *Mineral*
1152 *deposit models for resource assessment. US Geological Survey Scientific Investigations*
1153 *Report* 2010, 1-169.
- 1154 John, D.A., Taylor, R.D., 2016. By-products of porphyry copper and molybdenum
1155 deposits: Chapter 7.
- 1156 Kananian, A., Sarjoughian, F., Nadimi, A., Ahmadian, J., Ling, W., 2014. Geochemical
1157 characteristics of the Kuh-e Dom intrusion, Urumieh–Dokhtar Magmatic Arc (Iran):

- 1158 Implications for source regions and magmatic evolution. *Journal of Asian Earth Sciences*
1159 90, 137-148.
- 1160 Kaszuba, J.P., Janecky, D.R., Snow, M.G., 2005. Experimental evaluation of mixed fluid
1161 reactions between supercritical carbon dioxide and NaCl brine: Relevance to the integrity
1162 of a geologic carbon repository. *Chemical Geology* 217, 277-293.
- 1163 Keith, J.D., Shanks, W.C., Archibald, D.A., Farrar, E., 1986. Volcanic and intrusive
1164 history of the Pine Grove porphyry molybdenum system, southwestern Utah. *Economic*
1165 *Geology* 81, 553-577.
- 1166 Keppler, H., Wyllie, P.J., 1991. Partitioning of Cu, Sn, Mo, W, U, and Th between melt
1167 and aqueous fluid in the systems haplogranite-H₂O-HCl and haplogranite-H₂O-HF.
1168 *Contributions to Mineralogy and Petrology* 109, 139-150.
- 1169 Kerr, A., van Nostrand, T., Dickson, W., Lynch, E., 2009. Molybdenum and tungsten in
1170 Newfoundland: a geological overview and a summary of recent exploration
1171 developments. *Current Research, Newfoundland and Labrador Department of Natural*
1172 *Resources, Geological Survey, Report*, 09-01.
- 1173 Khaleghi, F., Hosseinzadeh, G., Rasa, I., Moayyed, M., 2013. Geological and
1174 Geochemical Characteristics of the Syah Kamar Porphyry Molybdenum Deposit, West
1175 of Mianeh, NW Iran. *ULUM-I ZAMIN* 88, 187-196.
- 1176 Khodabandeh, A.A., Amini Azar, R., Faridi, M., 1999. Geological map of the Mianeh
1177 quadrangle. *Geological Survey of Iran and Mining Exploration, Tehran*.
- 1178 Kim, H., Yang, K., Lentz, D., Jeong, H.-Y., Kil, Y., Hwang, J., Park, S.-G., 2016. Low-
1179 salinity Liquid-rich or Vapor-like fluids in a porphyry-type Mo deposit, South Korea.
1180 *The Canadian Mineralogist* 54, 715-736.
- 1181 Kirkland, C., Smithies, R., Taylor, R., Evans, N., McDonald, B., 2015. Zircon Th/U
1182 ratios in magmatic environs. *Lithos* 212, 397-414.
- 1183 Kirsch, K., Navarre-Sitchler, A.K., Wunsch, A., McCray, J.E., 2014. Metal release from
1184 sandstones under experimentally and numerically simulated CO₂ leakage conditions.
1185 *Environmental science & technology* 48, 1436-1442.
- 1186 Klemm, L.M., Pettke, T., Heinrich, C.A., 2008. Fluid and source magma evolution of the
1187 Questa porphyry Mo deposit, New Mexico, USA. *Mineralium Deposita* 43, 533.
- 1188 Knight, C., Bodnar, R., 1989. Synthetic fluid inclusions: IX. Critical PVTX properties of
1189 NaCl-H₂O solutions. *Geochimica et Cosmochimica Acta* 53, 3-8.
- 1190 Lawley, C., Richards, J., Anderson, R., Creaser, R., Heaman, L., 2010. Geochronology
1191 and geochemistry of the MAX porphyry Mo deposit and its relationship to Pb-Zn-Ag
1192 mineralization, Kootenay arc, southeastern British Columbia, Canada. *Economic*
1193 *Geology* 105, 1113-1142.
- 1194 Le Maitre, R.W., Streckeisen, A., Zanettin, B., Le Bas, M., Bonin, B., Bateman, P., 2005.
1195 *Igneous rocks: a classification and glossary of terms: recommendations of the*
1196 *International Union of Geological Sciences Subcommittee on the Systematics of*
1197 *Igneous Rocks*. Cambridge University Press.
- 1198 Lions, J., Devau, N., De Lary, L., Dupraz, S., Parmentier, M., Gombert, P., Dictor, M.-
1199 C., 2014. Potential impacts of leakage from CO₂ geological storage on geochemical
1200 processes controlling fresh groundwater quality: a review. *International Journal of*
1201 *Greenhouse Gas Control* 22, 165-175.

- 1202 Little, M.G., Jackson, R.B., 2010. Potential impacts of leakage from deep CO₂
1203 geosequestration on overlying freshwater aquifers. *Environmental science & technology*
1204 44, 9225-9232.
- 1205 Liu, F., Lu, P., Griffith, C., Hedges, S.W., Soong, Y., Hellevang, H., Zhu, C., 2012. CO₂-
1206 brine-caprock interaction: Reactivity experiments on Eau Claire shale and a review of
1207 relevant literature. *International Journal of Greenhouse Gas Control* 7, 153-167.
- 1208 Liu, J., Mao, J.-W., Wu, G., Wang, F., Luo, D.-F., Hu, Y.-Q., 2015. Geochemical
1209 signature of the granitoids in the Chalukou giant porphyry Mo deposit in the
1210 Heilongjiang Province, NE China. *Ore Geology Reviews* 64, 35-52.
- 1211 Ludington, S., Hammarstrom, J., Piatak, N., 2009. Low-fluorine stockwork molybdenite
1212 deposits. US Geological Survey Open- File Report 1211.
- 1213 Ludington, S., Plumlee, G.S., 2009. Climax-type porphyry molybdenum deposits. US
1214 Geological Survey.
- 1215 Ludwig, K., 2011. Isoplot v. 4.15: A Geochronological Toolkit for Microsoft Excel.
1216 Berkeley Geochronology Center Special Publication 4, 75.
- 1217 Mao, J., Wang, Y., Lehmann, B., Yu, J., Du, A., Mei, Y., Li, Y., Zang, W., Stein, H.J.,
1218 Zhou, T., 2006. Molybdenite Re-Os and albite ⁴⁰Ar/³⁹Ar dating of Cu-Au-Mo and
1219 magnetite porphyry systems in the Yangtze River valley and metallogenic implications.
1220 *Ore Geology Reviews* 29, 307-324.
- 1221 Mao, J.W., Pirajno, F., Xiang, J.F., Gao, J.J., Ye, H.S., Li, Y.F., Guo, B.J., 2011.
1222 Mesozoic molybdenum deposits in the east Qinling-Dabie orogenic belt: Characteristics
1223 and tectonic settings. *Ore Geology Reviews* 43, 264-293.
- 1224 Mao, J.W., Xie, G.Q., Bierlein, F., Qü, W.J., Du, A.D., Ye, H.S., Pirajno, F., Li, H.M.,
1225 Guo, B.J., Li, Y.F., Yang, Z.Q., 2008. Tectonic implications from Re-Os dating of
1226 Mesozoic molybdenum deposits in the East Qinling-Dabie orogenic belt. *Geochimica et*
1227 *Cosmochimica Acta* 72, 4607-4626.
- 1228 Massonne, H.-J., Opitz, J., Theye, T., Nasir, S., 2013. Evolution of a very deeply
1229 subducted metasediment from As Sifah, northeastern coast of Oman. *Lithos* 156, 171-
1230 185.
- 1231 McInnes, B., Evans, N., Belousova, E., Griffin, W., 2003. Porphyry copper deposits of
1232 the Kerman belt, Iran: timing of mineralization and exhumation processes. *Sci. Res. Rep.*
1233 *Australia. CSIRO* (41 pp).
- 1234 Mehrabi, B., Yardley, B., Cann, J., 1999. Sediment-hosted disseminated gold
1235 mineralisation at Zarshuran, NW Iran. *Mineralium Deposita* 34, 673-696.
- 1236 Mercer, C.N., Reed, M.H., Mercer, C.M., 2015. Time scales of porphyry Cu deposit
1237 formation: Insights from titanium diffusion in quartz. *Economic Geology* 110, 587-602.
- 1238 Mirnejad, H., Mathur, R., Hassanzadeh, J., Shafie, B., Nourali, S., 2013. Linking Cu
1239 mineralization to host porphyry emplacement: Re-Os ages of molybdenites versus U-Pb
1240 ages of zircons and sulfur isotope compositions of pyrite and chalcopyrite from the Iju
1241 and Sarkuh porphyry deposits in Southeast Iran. *Economic Geology* 108, 861-870.
- 1242 Mirnejad, H., Simonetti, A., Molasalehi, F., 2011. Pb isotopic compositions of some Zn-
1243 Pb deposits and occurrences from Urumieh-Dokhtar and Sanandaj-Sirjan zones in Iran.
1244 *Ore Geology Reviews* 39, 181-187.

- 1245 Moghadam, H.S., Rossetti, F., Lucci, F., Chiaradia, M., Gerdes, A., Martinez, M.L.,
1246 Ghorbani, G., Nasrabady, M., 2016. The calc-alkaline and adakitic volcanism of the
1247 Sabzevar structural zone (NE Iran): implications for the Eocene magmatic flare-up in
1248 Central Iran. *Lithos* 248, 517-535.
- 1249 Moritz, R., Ghazban, F., Singer, B.S., 2006. Eocene gold ore formation at Muteh,
1250 Sanandaj-Sirjan tectonic zone, Western Iran: a result of late-stage extension and
1251 exhumation of metamorphic basement rocks within the Zagros Orogen. *Economic
1252 Geology* 101, 1497-1524.
- 1253 Moritz, R., Rezeau, H., Ovtcharova, M., Tayan, R., Melkonyan, R., Hovakimyan, S.,
1254 Ramazanov, V., Selby, D., Ulianov, A., Chiaradia, M., Putlitz, B., 2016. Long-lived,
1255 stationary magmatism and pulsed porphyry systems during Tethyan subduction to post-
1256 collision evolution in the southernmost Lesser Caucasus, Armenia and Nakhitchevan.
1257 *Gondwana Research* 37, 465-503.
- 1258 Müller, A., Herklotz, G., Giegling, H., 2018. Chemistry of quartz related to the
1259 Zinnwald/Cínovec Sn-W-Li greisen-type deposit, Eastern Erzgebirge, Germany. *Journal
1260 of Geochemical Exploration* 190, 357-373.
- 1261 Nabatian, G., Li, X.-H., Wan, B., Honarmand, M., 2017a. The genesis of Mo-Cu deposits
1262 and mafic igneous rocks in the Senj area, Alborz magmatic belt, Iran. *Mineralogy and
1263 Petrology*, 1-20.
- 1264 Nabatian, G., Wan, B., Honarmand, M., 2017b. Whole rock geochemistry, molybdenite
1265 Re-Os geochronology, stable isotope and fluid inclusion investigations of the Siah-
1266 Kamar deposit, western Alborz-Azarbayjan: New constrains on the porphyry Mo deposit
1267 in Iran. *Ore Geology Reviews* 91, 638-659.
- 1268 Nabavi, M.H., 1976. An introduction to the geology of Iran. Geological survey of Iran
1269 109.
- 1270 Newberry, R., 1979. Polytypism in molybdenite (I); A non-equilibrium impurity-induced
1271 phenomenon. *American Mineralogist* 64, 758-767.
- 1272 Ni, P., Wang, G.-G., Yu, W., Chen, H., Jiang, L.-L., Wang, B.-H., Zhang, H.-D., Xu, Y.-
1273 F., 2015. Evidence of fluid inclusions for two stages of fluid boiling in the formation of
1274 the giant Shapinggou porphyry Mo deposit, Dabie Orogen, Central China. *Ore Geology
1275 Reviews* 65, 1078-1094.
- 1276 NICICO, 2009a. Geological report and map of Goydaraq area, at scale of 1:25000,
1277 Internal report.
- 1278 NICICO, 2009b. Geological report and map of Khatoon-Abad area, at scale of 1:25000,
1279 Internal report.
- 1280 NICICO, 2009c. Geological report and map of Siah-Kamar area, at scale of 1:25000,
1281 Internal report.
- 1282 NICICO, 2010. Geological report and map of Siah-Kamar area, at scale of 1:5000,
1283 Internal report.
- 1284 Oliver, N.H., Bons, P.D., 2001. Mechanisms of fluid flow and fluid-rock interaction in
1285 fossil metamorphic hydrothermal systems inferred from vein-wallrock patterns,
1286 geometry and microstructure. *Geofluids* 1, 137-162.

- 1287 Pettke, T., Oberli, F., Heinrich, C.A., 2010. The magma and metal source of giant
1288 porphyry-type ore deposits, based on lead isotope microanalysis of individual fluid
1289 inclusions. *Earth and Planetary Science Letters* 296, 267-277.
- 1290 Rezeau, H., Moritz, R., Wotzlaw, J.-F., Tayan, R., Melkonyan, R., Ulianov, A., Selby,
1291 D., d'Abzac, F.-X., Stern, R.A., 2016. Temporal and genetic link between incremental
1292 pluton assembly and pulsed porphyry Cu-Mo formation in accretionary orogens. *Geology*
1293 44, 627-630.
- 1294 Richards, J.P., 2015. Tectonic, magmatic, and metallogenic evolution of the Tethyan
1295 orogen: From subduction to collision. *Ore Geology Reviews* 70, 323-345.
- 1296 Richards, J.P., Sholeh, A., 2016. The Tethyan tectonic history and Cu-Au metallogeny of
1297 Iran, *Tectonics and Metallogeny of the Tethyan Orogenic Belt*, Society of Economic
1298 Geologists Special Publication, pp. 193-212.
- 1299 Richards, J.P., Wilkinson, D., Ullrich, T., 2006. Geology of the Sari Gunay epithermal
1300 gold deposit, northwest Iran. *Economic Geology* 101, 1455-1496.
- 1301 Rives, T., Rawnsley, K., Petit, J.-P., 1994. Analogue simulation of natural orthogonal
1302 joint set formation in brittle varnish. *Journal of Structural Geology* 16, 419-429.
- 1303 Robb, L., 2004. *Introduction to ore-forming processes*. Blackwell publishing.
- 1304 Rolland, Y., 2017. Caucasus collisional history: Review of data from East Anatolia to
1305 West Iran. *Gondwana Research* 49, 130-146.
- 1306 Rossetti, F., Tecce, F., Billi, A., Brilli, M., 2007. Patterns of fluid flow in the contact
1307 aureole of the Late Miocene Monte Capanne pluton (Elba Island, Italy): the role of
1308 structures and rheology. *Contributions to Mineralogy and Petrology* 153, 743-760.
- 1309 Rubatto, D., 2002. Zircon trace element geochemistry: partitioning with garnet and the
1310 link between U-Pb ages and metamorphism. *Chemical Geology* 184, 123-138.
- 1311 Sarjoughian, F., Kananian, A., 2017. Zircon U-Pb geochronology and emplacement
1312 history of intrusive rocks in the Ardestan section, central Iran. *Geologica acta* 15, 0025-
1313 0036.
- 1314 Sarjoughian, F., Kananian, A., Haschke, M., Ahmadian, J., Ling, W., Zong, K., 2012.
1315 Magma mingling and hybridization in the Kuh-e Dom pluton, Central Iran. *Journal of*
1316 *Asian Earth Sciences* 54-55, 49-63.
- 1317 Seedorff, E., Dilles, J.H., Proffett, J.J.M., Einaudi, M.T., Zurcher, L., Stavast, W.J.A.,
1318 Johnson, D.A., Barton, M.D., 2005. *Porphyry Deposits: Characteristics and Origin of*
1319 *Hypogene Features*, In: Hedenquist, J.W., Thompson, J.F.H., Goldfarb, R.J., Richards,
1320 J.P. (Eds.), *One Hundredth Anniversary Volume*. Society of Economic Geologists.
- 1321 Seedorff, E., Einaudi, M.T., 2004. Henderson porphyry molybdenum system, Colorado:
1322 II. Decoupling of introduction and deposition of metals during geochemical evolution of
1323 hydrothermal fluids. *Economic Geology* 99, 39-72.
- 1324 Selby, D., Creaser, R.A., 2001. Re-Os geochronology and systematics in molybdenite
1325 from the Endako porphyry molybdenum deposit, British Columbia, Canada. *Economic*
1326 *Geology* 96, 197-204.
- 1327 Selby, D., Creaser, R.A., 2004. Macroscale NTIMS and microscale LA-MC-ICP-MS Re-
1328 Os isotopic analysis of molybdenite: Testing spatial restrictions for reliable Re-Os age
1329 determinations, and implications for the decoupling of Re and Os within molybdenite.
1330 *Geochimica et Cosmochimica Acta* 68, 3897-3908.

- 1331 Selby, D., Nesbitt, B.E., Muehlenbachs, K., Prochaska, W., 2000. Hydrothermal
1332 alteration and fluid chemistry of the Endako porphyry molybdenum deposit, British
1333 Columbia. *Economic Geology* 95, 183-202.
- 1334 Seo, J.H., Guillong, M., Heinrich, C.A., 2012. Separation of molybdenum and copper in
1335 porphyry deposits: The roles of sulfur, redox, and pH in ore mineral deposition at
1336 Bingham Canyon. *Economic Geology* 107, 333-356.
- 1337 Shafiei, B., Haschke, M., Shahabpour, J., 2009. Recycling of orogenic arc crust triggers
1338 porphyry Cu mineralization in Kerman Cenozoic arc rocks, southeastern Iran.
1339 *Mineralium Deposita* 44, 265.
- 1340 Shafiei, B., Shahabpour, J., Haschke, M., 2008. Transition from Paleogene normal calc-
1341 alkaline to Neogene adakitic-like plutonism and Cu-metallogeny in the Kerman porphyry
1342 copper belt: response to Neogene crustal thickening. *Journal of Sciences, Islamic
1343 Republic of Iran* 19, 67-84.
- 1344 Shahabpour, J., Kramers, J., 1987. Lead isotope data from the Sar-Cheshmeh porphyry
1345 copper deposit, Iran. *Mineralium Deposita* 22, 278-281.
- 1346 Shahsavari Alavijeh, B., Rashidnejad-Omran, N., Corfu, F., 2017. Zircon U-Pb ages and
1347 emplacement history of the Nodoushan plutonic complex in the central Urumieh-Dokhtar
1348 magmatic belt, Central Iran: Product of Neotethyan subduction during the Paleogene.
1349 *Journal of Asian Earth Sciences* 143, 283-295.
- 1350 Shannon, J., Walker, B., Carten, R., Geraghty, E., 1982. Unidirectional solidification
1351 textures and their significance in determining relative ages of intrusions at the Henderson
1352 Mine, Colorado. *Geology* 10, 293-297.
- 1353 Shinohara, H., Kazahaya, K., Lowenstern, J.B., 1995. Volatile transport in a convecting
1354 magma column: Implications for porphyry Mo mineralization. *Geology* 23, 1091-1094.
- 1355 Sillitoe, R.H., 2010. Porphyry copper systems. *Economic Geology* 105, 3-41.
- 1356 Simmonds, V., Moazzen, M., 2015. Re-Os dating of molybdenites from Oligocene Cu-
1357 Mo-Au mineralized veins in the Qarachilar area, Qaradagh batholith (northwest Iran):
1358 implications for understanding Cenozoic mineralization in South Armenia, Nakhchivan,
1359 and Iran. *International Geology Review* 57, 290-304.
- 1360 Simmonds, V., Moazzen, M., Selby, D., 2017. Re-Os dating of mineralization in Siah
1361 Kamar porphyry Mo deposit (NW Iran) and investigating on its temporal relationship
1362 with porphyry Cu-Mo deposits in the southern Lesser Caucasus, NW and central Iran,
1363 EGU General Assembly Conference Abstracts, p. 665.
- 1364 Simmonds, V., Moazzen, M., Selby, D., 2019. U-Pb zircon and Re-Os molybdenite age
1365 of the Siah Kamar porphyry molybdenum deposit, NW Iran. *International Geology
1366 Review*, 1-17.
- 1367 Sinclair, W., 2007. Porphyry deposits. *Mineral deposits of Canada: A synthesis of major
1368 deposit-types, district metallogeny, the evolution of geological provinces, and exploration
1369 methods: Geological Association of Canada, Mineral Deposits Division, Special
1370 Publication* 5, 223-243.
- 1371 Smoliar, M.I., Walker, R.J., Morgan, J.W., 1996. Re-Os ages of group IIA, IIIA, IVA,
1372 and IVB iron meteorites. *Science* 271, 1099-1102.
- 1373 Stein, H., Markey, R., Morgan, J., Hannah, J., Scherstén, A., 2001. The remarkable Re-
1374 Os chronometer in molybdenite: how and why it works. *Terra Nova* 13, 479-486.

- 1375 Stocklin, J., 1968. Structural history and tectonics of Iran: a review. *AAPG Bulletin* 52,
1376 1229-1258.
- 1377 Sutulov, A., 1973. Mineral resources and the economy of the USSR. Backbeat Books.
- 1378 Taghipour, N., Aftabi, A., Mathur, R., 2008. Geology and Re-Os Geochronology of
1379 Mineralization of the Miduk Porphyry Copper Deposit, Iran. *Resource Geology* 58, 143-
1380 160.
- 1381 Taylor, R.D., Hammarstrom, J.M., Piatak, N.M., Seal II, R.R., 2012. Arc-related
1382 porphyry molybdenum deposit model: Chapter D in Mineral deposit models for resource
1383 assessment. US Geological Survey.
- 1384 Ulrich, T., Mavrogenes, J., 2008. An experimental study of the solubility of molybdenum
1385 in H₂O and KCl-H₂O solutions from 500 °C to 800 °C, and 150 to 300 MPa. *Geochimica
1386 et Cosmochimica Acta* 72, 2316-2330.
- 1387 Verdel, C., Wernicke, B.P., Hassanzadeh, J., Guest, B., 2011. A Paleogene extensional
1388 arc flare-up in Iran. *Tectonics* 30.
- 1389 Villa, I.M., De Bièvre, P., Holden, N., Renne, P., 2015. IUPAC-IUGS recommendation
1390 on the half life of ⁸⁷Rb. *Geochimica et Cosmochimica Acta* 164, 382-385.
- 1391 Wallace, S., 1995. The Climax-type molybdenite deposits: what they are, where they are
1392 and why they are. *Economic Geology* 90, 1359-1380.
- 1393 Wan, B., Deng, C., Najafi, A., Hezareh, M.R., Talebian, M., Dong, L., Chen, L., Xiao,
1394 W., 2018. Fertilizing porphyry Cu deposits through deep crustal hot zone melting.
1395 *Gondwana Research* 60, 179-185.
- 1396 Wang, G., Wu, G., Xu, L., Li, X., Zhang, T., Quan, Z., Wu, H., Li, T., Liu, J., Chen, Y.,
1397 2017. Molybdenite Re-Os age, H-O-C-S-Pb isotopes, and fluid inclusion study of the
1398 Caosiyao porphyry Mo deposit in Inner Mongolia, China. *Ore Geology Reviews* 81, 728-
1399 744.
- 1400 Wark, D.A., Watson, E.B., 2006. TitaniQ: a titanium-in-quartz geothermometer.
1401 *Contributions to Mineralogy and Petrology* 152, 743-754.
- 1402 Westra, G., Keith, S.B., 1981. Classification and genesis of stockwork molybdenum
1403 deposits. *Economic Geology* 76, 844-873.
- 1404 Whitcher, I., 1975. Anduramba molybdenum prospect, *Economic Geology of Australia
1405 and Papua New Guinea. 1—Metals*, pp. 793-794.
- 1406 Whitney, D.L., Evans, B.W., 2010. Abbreviations for names of rock-forming minerals.
1407 *American Mineralogist* 95, 185-187.
- 1408 Wiedenbeck, M., Alle, P., Corfu, F., Griffin, W., Meier, M., Oberli, F.v., Quadt, A.v.,
1409 Roddick, J., Spiegel, W., 1995. Three natural zircon standards for U-Th-Pb, Lu-Hf,
1410 trace element and REE analyses. *Geostandards Newsletter* 19, 1-23.
- 1411 Wilkinson, J., 2001. Fluid inclusions in hydrothermal ore deposits. *Lithos* 55, 229-272.
- 1412 Wilkinson, J.J., 2013. Triggers for the formation of porphyry ore deposits in magmatic
1413 arcs. *Nature Geoscience* 6, 917-925.
- 1414 Wu, Y.-S., Chen, Y.-J., Zhou, K.-F., 2017. Mo deposits in Northwest China: Geology,
1415 geochemistry, geochronology and tectonic setting. *Ore Geology Reviews* 81, 641-671.

- 1416 Xiaoyun, C., 1989. Solubility of molybdenite and the transport of molybdenum in
1417 hydrothermal solutions. Ph. D. thesis. Iowa State University, 1~ 111.
- 1418 Xue, C., Chi, G., Zhao, X., Wu, G., Zhao, Z., Dong, L., 2016. Multiple and prolonged
1419 porphyry Cu–Au mineralization and alteration events in the Halasu deposit, Chinese
1420 Altai, Xinjiang, northwestern China. *Geoscience Frontiers* 7, 799-809.
- 1421 Yang, Z., 2007. Re-Os isotopic ages of Tangjiaping molybdenum deposit in Shangcheng
1422 County, Henan and their geological significance. *Kuangchuang Dizhi(Mineral Deposits)*
1423 26, 289-295.
- 1424 Yeganehfar, H., Ghorbani, M.R., Shinjo, R., Ghaderi, M., 2013. Magmatic and
1425 geodynamic evolution of Urumieh–Dokhtar basic volcanism, Central Iran: major, trace
1426 element, isotopic, and geochronologic implications. *International Geology Review* 55,
1427 767-786.
- 1428 Zeng, Q.-D., Sun, Y., Chu, S.-X., Duan, X.-X., Liu, J., 2015. Geochemistry and
1429 geochronology of the Dongshanwan porphyry Mo–W deposit, Northeast China:
1430 implications for the Late Jurassic tectonic setting. *Journal of Asian Earth Sciences* 97,
1431 472-485.
- 1432 Zeng, Q., Liu, J., Chu, S., Wang, Y., Sun, Y., Duan, X., Zhou, L., 2012. Mesozoic
1433 molybdenum deposits in the East Xingmeng orogenic belt, northeast China:
1434 characteristics and tectonic setting. *International Geology Review* 54, 1843-1869.
- 1435 Zhai, D., Liu, J., Tombros, S., Williams-Jones, A.E., 2017. The genesis of the Hashitu
1436 porphyry molybdenum deposit, Inner Mongolia, NE China: constraints from
1437 mineralogical, fluid inclusion, and multiple isotope (H, O, S, Mo, Pb) studies.
1438 *Mineralium Deposita* 53, 377-397.
- 1439 Zhang, X., Lentz, D.R., Yao, C., Liu, R., Yang, Z., Mei, Y., Fan, X., Huang, F., Qin, Y.,
1440 Zhang, K., 2018. Geochronology, geochemistry, and Sr–Nd–Pb–Hf isotopes of the
1441 Zhunsujihua granitoid intrusions associated with the molybdenum deposit, northern Inner
1442 Mongolia, China: implications for petrogenesis and tectonic setting. *International Journal*
1443 *of Earth Sciences* 107, 687-710.
- 1444 Zhang, Y.-G., Frantz, J.D., 1987. Determination of the homogenization temperatures and
1445 densities of supercritical fluids in the system NaClKClCaCl₂H₂O using synthetic fluid
1446 inclusions. *Chemical Geology* 64, 335-350.
- 1447 Zindler, A., Hart, S., 1986. Chemical geodynamics. *Annual review of earth and planetary*
1448 *sciences* 14, 493-571.

1449

1450 **Figures captions**

- 1451 Figure 1: Simplified tectono-geological map of Iran with the main Cu, Au and Mo ore
1452 deposits and their ages. Based on maps from the (Huber, 1977), with additional information
1453 from (Berberian and King, 1981) and Richards et al. (2012). See also Table 1 for the
1454 references for each mineralisation site.

1455 Figure 2: Simplified geological map of Mianeh-Hashtroud region, as derived from field
 1456 and remote sensing investigations (modified after Amidi et al., 1987; NICICO, 2009c, b, a).

1457 Figure 3: Top: Geological-alteration map of the Siah-Kamar Mo deposit (see Fig. 3 for
 1458 map location). The ellipse indicates the estimated alteration zone. Bottom: Interpretative
 1459 geological cross section across the Mo ore deposit, also showing distribution of the main
 1460 alteration types. Abbreviations: Ab, Albite; Act, Actinolite; Ap, Apatite; Bt, Biotite, Cal,
 1461 Calcite; Chl, Chlorite; Ep, Epidote; ill, Illite. Kal, Kaolinite; Kfs, K-feldspar; Mag,
 1462 Magnetite; Or, Orthose, Psp, Paraspurite; Po, Pyrrhotite; Py, Pyrite; Qtz, Quartz; Sch,
 1463 Scheelite; Ser, Sericite.

1464 Figure 4: General field view of the Siah-Kamar Mo deposit area (field of view 2.5 km).
 1465 The line drawing illustrates the main rock and alteration types. Abbreviations: alt., alteration;
 1466 Cb, carbonate; K, Potassic; mp, mineralized basic/intermediate porphyry rocks.

1467 Figure 5: Rock textures and alterations. (a) The textural appearance of the potassic-sodic
 1468 alteration within the main mineralised porphyry body in the outcrop. Alteration mineralogy
 1469 consists of Bt-Fsp+ Po, Mg assemblage overprinting early igneous phases. (b) potassic-sodic
 1470 alteration at the thin section scale (plane polarised light). (c) Back-scattered electron (BSE)
 1471 image showing disseminated molybdenite flakes within the secondary feldspar-biotite
 1472 assemblage. (d) Biotite veinlets in the potassic-sodic alteration zone overprinted by Kfs-Qz
 1473 veins (plane polarised light). (e) BSE image showing early magnetite inclusions in secondary
 1474 feldspar and ilmenite inclusions in texturally-late biotite. (f) Brecciated andesite country
 1475 rocks and epidote veining within the propylitic alteration zone. (g) General appearance of the
 1476 phyllic and argillic alteration zones. (h) Rock slab from phyllic/silicified zones showing the
 1477 development of Qz + Py veins with sericitic halos; (i-j) Microtexture of volcanic country rock
 1478 within pronounced phyllic alteration made of Qz + Ser + Py assemblage (crossed polars).

1479
 1480 Figure 6: (a) The contact between the mineralised porphyry body and the country rocks.
 1481 Note the presence of potassic alteration and intense veining within the porphyry body and
 1482 how the veining dies out abruptly across the contact (see also the interpretative line drawing
 1483 in the inset). (b) Rose diagram of the cumulative vein strikes as measured within the different
 1484 alteration zones. (c) Contour diagram of the cumulative poles to Mo-mineralised veins (V2a
 1485 and V2b) within the potassic-sodic alteration zone (Equal area Schmidt net, lower

1486 hemisphere projection). (d) Contour diagram of the poles to (V2b) Cb-Mo veins within the
1487 potassic-sodic alteration zone (Equal area Schmidt net, lower hemisphere projection). (e)
1488 Contour diagram of the poles to epidote (Ep) veins within the propylitic alteration zone
1489 (Equal area Schmidt net, lower hemisphere projection).

1490 **Figure 7.** Conceptual model for veining and Mo mineralisation within the potassic-sodic
1491 alteration zone (see text for further details).

1492 **Figure 8.** (a) Rock slab of an early Qz-Kfs-Ab V2a vein with V2b Mol-bearing carbonate
1493 mineral assemblages growing in pre-existing vugs. Note the marginal K-feldspar + albite
1494 selvage. (b) BSE image showing the textural appearance of a V2a Qz-Kfs vein overprinted by
1495 a late, post-ore Fe-oxide vein. Molybdenite occurs in the centre of the vein. (c) BSE image
1496 showing coexisting scheelite (Sch) and Mol within V2a Qz + Kfs vein.

1497 **Figure 9.** (a) Rock slabs of composite V2a-V2b veins showing different degree of the
1498 textural overprinting operated by the Cb-Mol mineralisation. (b) BSE image showing V2b
1499 veining overprinting early V2a Qz, sericite halos and compositional zoning in Cb. (c) BSE
1500 image showing a ribbon texture along margins of a V2b vein, attesting episodic Cb-Mol
1501 precipitation. (d) BSE image showing the textural overprint operated by the V2b Cb-Mo
1502 veining onto pre-existing Qz-Kfs V2a one. Sericite formed after alteration of Kfs. Note the
1503 reworking of the Qz grain boundary during V2b veining.

1504 **Figure 10:** Mineralization stages and their associated mineral assemblages in the SKMD.

1505 **Figure 11.** Representative discrimination diagrams for quartz chemistry (after Müller et
1506 al., 2018) as derived from in situ LA-ICPMS analyses of quartz grains from V2a veins. (a) Li
1507 vs Al. (b) Al vs Ge. (c) Al vs Li.

1508 **Figure 12:** Microphotographs of the fluid inclusions types hosted in V2a-V2b veins. (a)
1509 Type A1 (two-phase L-rich) fluid inclusions in Qz (V2a vein). (b) Type A2 (two-phase L-
1510 rich) fluid inclusions in Qz (V2a vein). (c) Type A3 (two-phase L-rich) fluid inclusions in
1511 Qz-Py vein from the phyllic alteration zone. (d) Type A4 (two-phase L-rich) fluid inclusions
1512 in Psp (V2b Vein). Type B solid-bearing fluid inclusions in Qz (V2a vein).

1513 **Figure 13.** (a) and (b) Representative Raman spectra from fluid and gas phases from
1514 types A1 fluid inclusions in Qz from V2a veins.

1515 Figure 14. Histogram of homogenization temperature (Th) (a) and salinity (b) for the
1516 analysed fluid inclusion types.

1517 Figure 15. (a, c, e and g) Cathodoluminescence images from the analysed zircon grains,
1518 with location of the laser spots (circles and relative id numbers in parenthesis) and obtained
1519 $^{206}\text{Pb}/^{238}\text{U}$ ages (2σ error; Ma). Spots that provided inherited zircon ages are denoted by
1520 dashed circles. (b) Tera-Wasserburg concordia diagram for sample MN03 (d, f, h).
1521 Conventional Concordia diagrams with Concordia ages indicated (2σ error; Ma) for the
1522 MN01, MN19, and MN31 samples. See also Table 5 for the corresponding analytical results.

1523 Fig 16: Mineral data and Rb–Sr age results for sample MN02. Analytical data are given
1524 in Table 7. Grain size is indicated when different grain size fractions were analyzed. Kfs, K-
1525 feldspar.

1526 Figure 17: (a) Calculated Isochores for the representative type-A1 (quartz) and -A4
1527 (paraspurrite) fluid inclusions (BULK and ISOC software; Bakker, 2003), combined with
1528 isopleths as obtained from Ti-in-quartz thermometry. (b) Salinity versus homogenization
1529 temperature (Th) diagram for all the FI types. Dashed arrows indicate the possible fluid
1530 evolution. (c) Schematic diagram showing typical trends in a Th-salinity space for fluid
1531 evolution in hydrothermal ore deposits (after Wilkinson, 2001).

1532 Figure 18: (a) A model for the Mo mineralisation at Siah-kamar framed within a scenario
1533 of long-lived thermal anomaly and magmatism. (a) Stage-1 mineralisation (33Ma).
1534 Emplacement of the basic/intermediate porphyry body with pervasive potassic-sodic
1535 alteration and low-grade disseminated Mo mineralization. (b) Emplacement of a new batch of
1536 acidic magmas (at 29-28 Ma) caused re-fertilisation of the intrusive/cap rock system, with
1537 formation of V2a veining (stage-2a). (c) The main mineralisation stage (29-28 Ma). The
1538 continuous exsolution of acidic, CO₂-bearing fluid from the new magma products caused
1539 leaching of the early deposited Mo and, by neutralisation due to the interaction with meteoric
1540 fluids, the high-grade Mo mineralization during structurally-controlled stockwork Cb veining
1541 (stage-2b).

1542

1543 Table 1. List of the studied samples with their location, petrographical characteristic and
1544 analytical methods adopted.

S	Ro	Rock texture and	Alteration	Locati	Method
---	----	------------------	------------	--------	--------

Sample	Rock Type	Petrography	Alteration Type	Temperature (decimal degree)	EPMA	LA-	Zircon	Mol.	Rb-Sr
N01	Mylonitic	Porphyritic with microgranular groundmass. Qz (5-10 %), Pl+Kfs (5-10 %) phenocrysts. Groundmass: Qz (20-30 %), KFsp (40-50 %), Pl (10-15 %), Biotite (<5 %).	Weakly phyllic alteration. Qz veins, rare Ser, Py and Fe-oxides	N: 37.41297 E: 47.59745					
N02	Mylonitic (Dioritic)	Porphyritic with microgranular groundmass. Magmatic texture mostly overprinted. Relic Pl (20-30 %) phenocrysts and pseudomorphous secondary aggregates after Cpx (5-10 %).	Strong sodic-potassic alteration. Disseminated secondary fine grained Ab+Kfs+Qtz+Bt+Mag (40-50%), Qz-Afs-Mol-Cb-Rt-Sch veins (5-10 %)	N: 37.39916 E: 47.59519		*			
N19	Mylonitic	Porphyritic with glassy groundmass. Glass (50-60 %), euhedral to subhedral Pl (20-25 %), Bt (5-7 %), Amph (2-3 %), Qz (5-7 %) phenocrysts.	Almost unaltered; secondary Chlorite on Amph	N: 37.39925 E: 47.58888					

<p>A andesit oid/Ba saltoid M (Diorit N31 e to monzo diorite porphy ry)</p>	<p>Porphyritic with microgranular groundmass. Pl (30-35) , Cpx (15-20 %) phenocrysts. Groudnmass: Pl (25-30) , Cpx (15-20 %)+ Mag (4-6 %),</p>	<p>Propylitic alteration. Ep (10-15 %)+ Act/Tr (5-10) , Py</p>	<p>N: 37.38710 E: 47.60161</p>
<p>A andesit oid/Ba M saltoid N65 (monz odiorit e)</p>	<p>Porphyritic with microgranular groundmass. Pl (20-30) , Cpx (7-10 %), Opx (5 %) phenocrysts. Groundmass: Pl+KFs+Px+Mag (40-50)</p>	<p>Weakly propylitic alteration. Cb (disseminated over mafic minerals and Pl) and Cb veining (2-3) , secondary Chl on Cpx and Opx.</p>	<p>N: 37.406533 E: 47.589648</p>
<p>A andesit oid/Ba M saltoid N55 (monz onite porphy ry)</p>	<p>Porphyritic with microgranular groundmass. Pl (5-7 %) phenocrysts. Groudnmass: Pl (60-70), KFs (5-10? %), Mag (5- 7 %).</p>	<p>Weakly altered to Cb</p>	<p>N: 37.40281 E: 47.59006</p>

1547 Table 2. Trace element chemistry of quartz from V2 veins

Sp ot	Li	B	Al	M n	G a	G e	A s
ppm							
v4	3.2	3.	35.	0	0	0	0
q	6	90	97	.15	.10	.89	.01
v4	24.	5.	15	1	0	1	2
a2	52	18	6.97	.05	.11	.41	.02
v4	3.3	3.	98.	0	0	1	1
b2	4	57	49	.70	.13	.20	.77
v4	6.5	8.	89.	0	0	1	0
c2	0	35	96	.27	.01	.98	.94
v4	28.	7.	16	0	0	1	0
d2	03	63	0.22	.20	.06	.87	.80
v4	1.8	4.	45.	0	<i>b</i>	<i>b</i>	0
e2	6	58	10	.24	<i>dl</i>	<i>dl</i>	.14
v4	17.	4.	10	0	0	1	<i>b</i>
f2	07	00	2.47	.66	.17	.33	<i>dl</i>

bdl: Below detection limit

1548

1549

16.

1551 Table 3. Ti-in-Quartz content and results of TitaniQ thermometry (V2 veins)

S pot	Ti (ppm)	Temperature (°C) calculated for P (kbar)				
		0.	1	1.	2	2.
		5	5	5	5	5
v	21.1	4	5	5	5	5
4b	7	94	27	50	69	85
v	21.5	4	5	5	5	5
4c	2	95	28	51	70	86
v	31.8	5	5	5	6	6
4d	8	27	61	85	05	21
v	29.7	5	5	5	5	6
4e	8	21	55	79	99	15
v	17.4	4	5	5	5	5
4f	2	79	11	34	53	68
v	44.2	5	5	6	6	6
4g	0	55	91	16	36	53
v	45.0	5	5	6	6	6
4i	0	57	92	18	38	55
v	20.9	4	5	5	5	5
4j	1	93	26	49	68	83
v	44.6	5	5	6	6	6
4n	9	56	92	17	37	54
v	17.3	4	5	5	5	5
4q	6	79	11	34	52	68
v	54.6	5	6	6	6	6
4a2	5	75	11	37	57	75
v	41.6	5	5	6	6	6
4b2	6	50	85	10	30	47

v	24.5	5	5	5	5	5
4c2	7	05	39	63	81	98
v	48.0	5	5	6	6	6
4d2	2	63	98	24	44	61
v	23.6	5	5	5	5	5
4e2	1	02	36	59	78	94
v	24.6	5	5	5	5	5
4f2	7	06	39	63	82	98

1552

ACCEPTED MANUSCRIPT

Table 4. Summary of the FI characteristics and the obtained microthermometry results

T type	V to L ratio	H ost minera l	A lterat ion zone	M easur ed numb er	T freezing (°C)	T eutectic (°C)	T homogen ization (°C)	T melting (°C)	S alinit y (wt.% NaCl eq.)
T A1 (L- rich+ V)	0 .5-1	Q uartz	P otass ic	4 4	44.4 to - 29.6 (Mean= -38.5)	- -30 to -22.5 (Mean= -25.3)	298 to 365 (Mean= 333)	- 4,3 to - 0,6 (Mean= -2)	1 to 6,9 (Mod e= 3.85)
T A2 (L- rich+ V)	0 .1- 0.4	Q uartz	P otass ic	1 95	47.2 to - 25.3 (Mean= -39)	- - 31.5 to -23 (Mode= -23)	170 to 352 (Mean= 272)	- 3.7 to - 0.1 (Mean= -1.5)	0. 2 to 6 (Mea n= 2.6)
T A3 (L- rich+ V)	0 .2- 0.4	Q uartz	P hylli c	5 2	41.4 to - 31 (Mean= -33.6)	- -22 to -21 (Mean= -21.5)	232 to 365 (Mode= 320)	- 2,6 to - 1 (Mean= -1.8)	1. 7 to 4.3 (Mea n= 3.1)
T A4 (L- rich+ V)	0 .1- .25	Pa raspurr ite	P otass ic	9 1	-30 to -42 (Mean= -39)	-24 to -33 (Mean= -27)	145 to 300 (Mode= 225)	- 1,2 to - 0,1 (Mean= -0.35)	0. 2 to 2.1 (Mea n= 0.6)

T						-25			
ype B	0		P			to -65			3
(L-	.1-	Q	otass	4	-80	(Mean=	203	-34	0.5 to
rich+	0.2	uartz	ic		to -39.8	-28.5	to 320	to -11.5	32
V±S)						and -			
						61)			

1555

ACCEPTED MANUSCRIPT

1558	1559	1560	1561	1562	1563	1564	1565	1566	1567	1568	1569	1570	1571	1572	1573	1574	1575	1576	1577	1578	1579	1580	1581	1582	1583	1584	1585	1586	1587	1588	1589	1590	1591	1592	1593	1594	1595	1596	1597	1598	1599	1600
------	------	------	------	------	------	------	------	------	------	------	------	------	------	------	------	------	------	------	------	------	------	------	------	------	------	------	------	------	------	------	------	------	------	------	------	------	------	------	------	------	------	------

* 206 Percentage of Pb contributed by common Pb on the basis of 204 Pb. Value of common Pb was assumed by Stacey and Kramers (1975) model; n.d.: no detection of 204Pb

** Degree of discordance (%); negative numbers and blanks show normal discordant and concordant within 2 σ of the analytical error, respectively.

ACCEPTED MANUSCRIPT

1561 Table 6. Re-Os isotopic data for two molybdenite samples from the Siah-Kamar Mo deposit

Sample	w t (g)	Re(ppm)	¹⁸⁷ Re(ppm)	¹⁸⁷ Os (ppb)	A ge	*	#
RO780- 13_Mo1B	0 .016	19. 33	12.15 .09	5.81 .05	2 8.70	.14	.17
RO780- 14_Mo2B	0 .016	22. 14	13.92 .10	6.56 .06	2 8.29	.14	.16

1562 *uncertainty including all sources of analytical uncertainty

1563 #uncertainty including all sources of analytical uncertainty plus decay constant

1565 Table 7. Rb-Sr analytical data for the mineral separated from sample MN02

Ana lysis	material	Rb ppm	Sr ppm	$^{87}\text{Rb}/^{86}\text{Sr}$	$^{87}\text{Sr}/^{86}\text{Sr}$	$^{87}\text{Sr}/^{86}\text{Sr} \ 2\sigma_m$ (%)
PS3 104	biotite	306	19 4	4.56	0.70 7085	0.0019
PS3 105	kfsp >160 μm	138	87 5	0.45 5	0.70 5176	0.0011
PS3 106	sericite >125 μm	397	11 8	9.73 2	0.70 8913	0.0015
PS3 107	kfsp <160 μm	145	89 3	0.47 1	0.70 5179	0.0008
PS3 108	sericite <125 μm	375	19 0	5.72	0.70 7161	0.0022
PS3 109	apatite conc.	91. 2	65 2	0.40 5	0.70 5162	0.0021

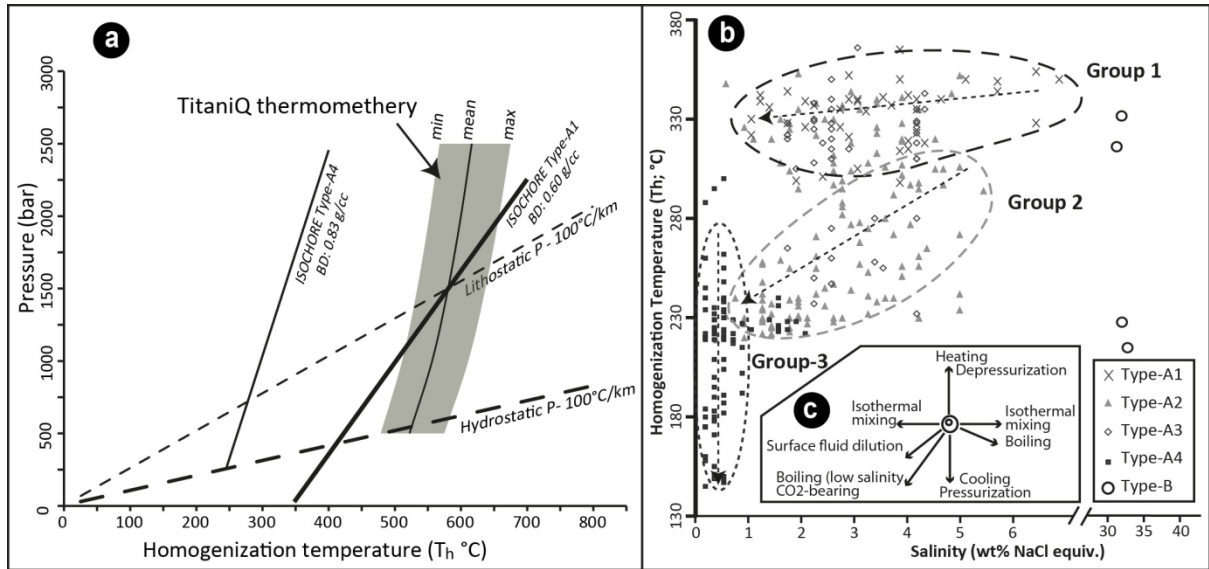
1566

1567

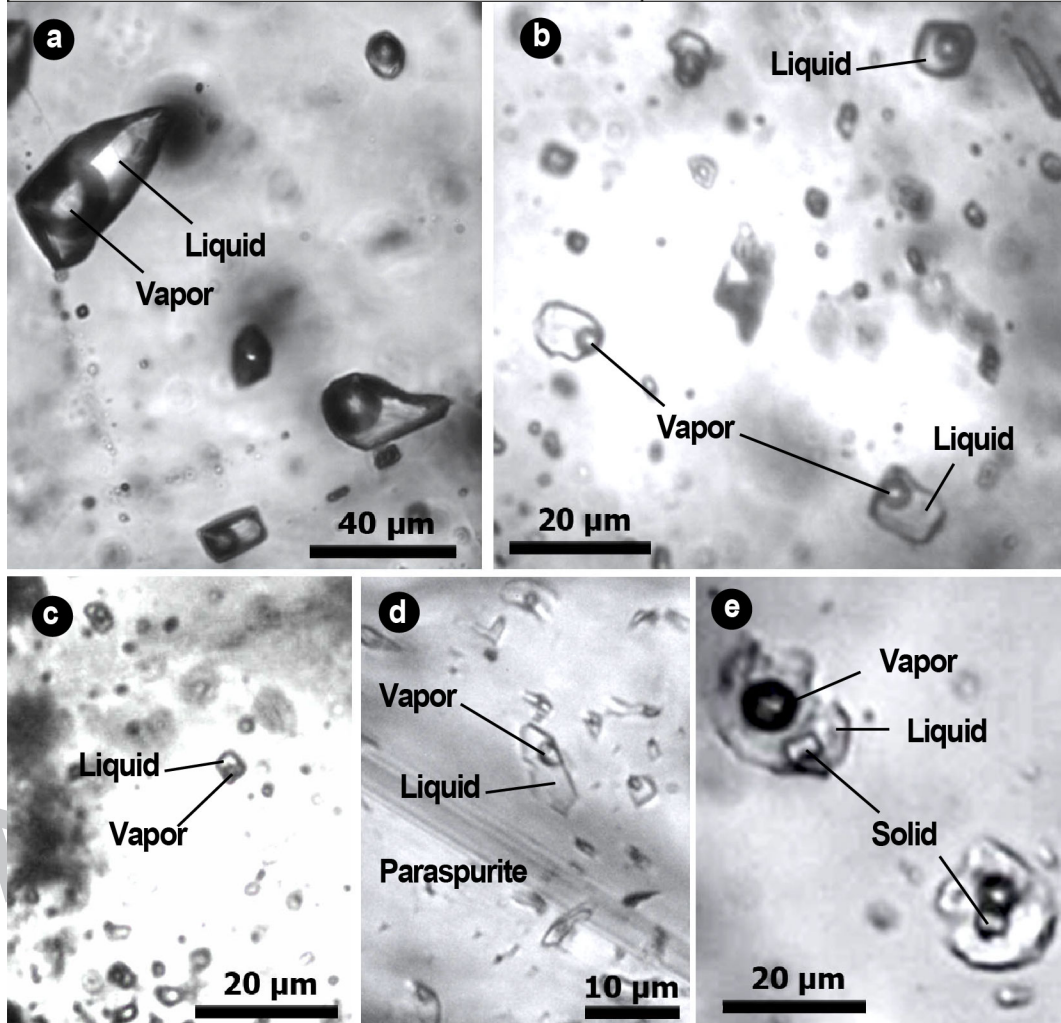
1568

1569

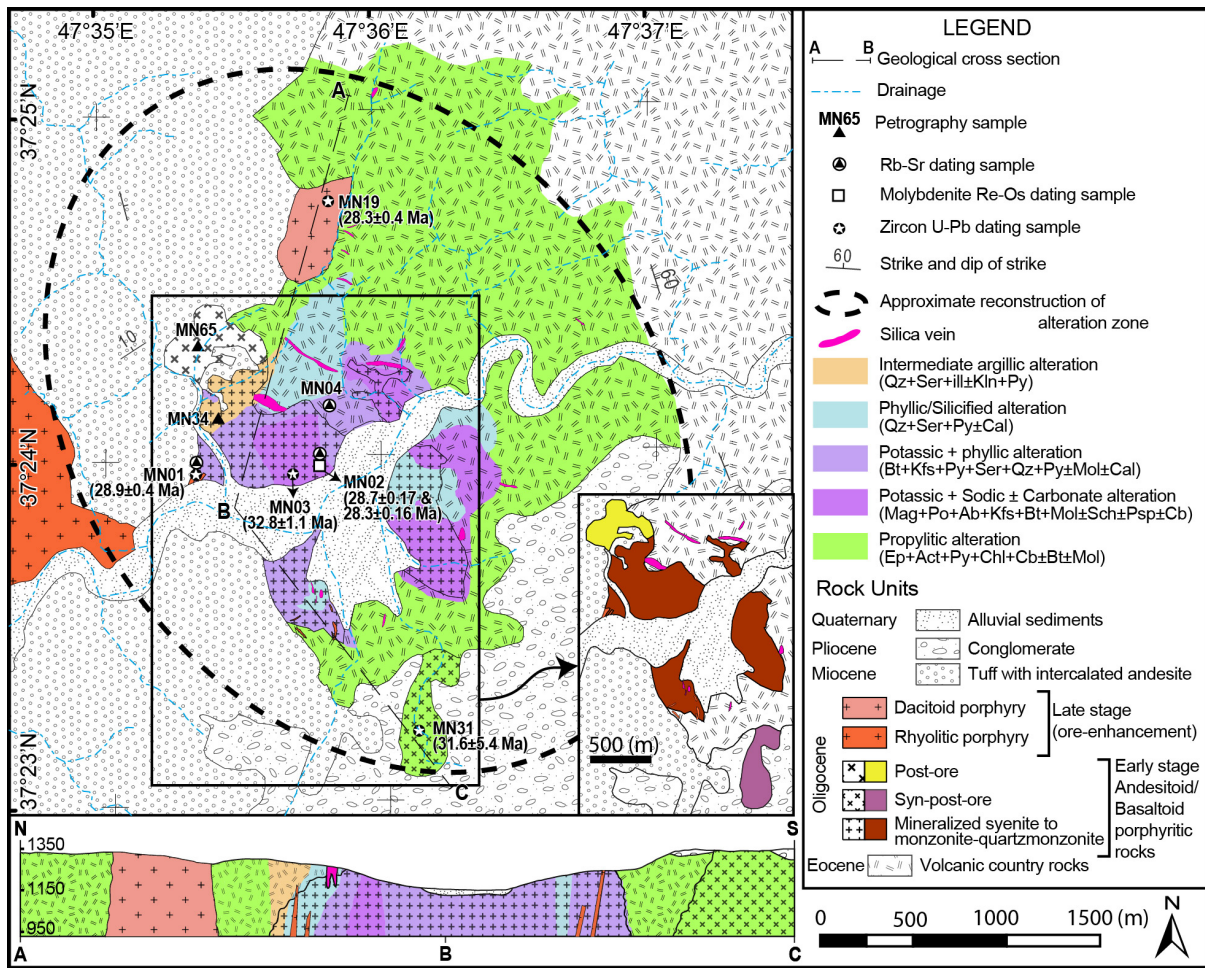
1570



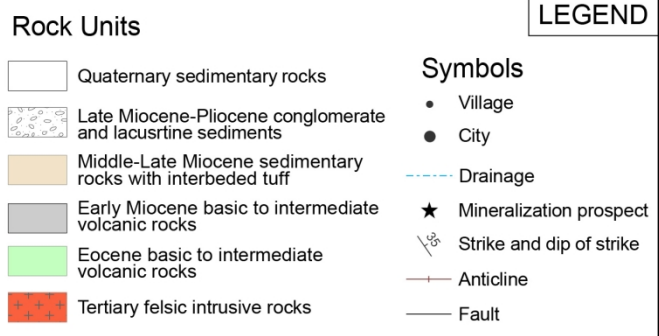
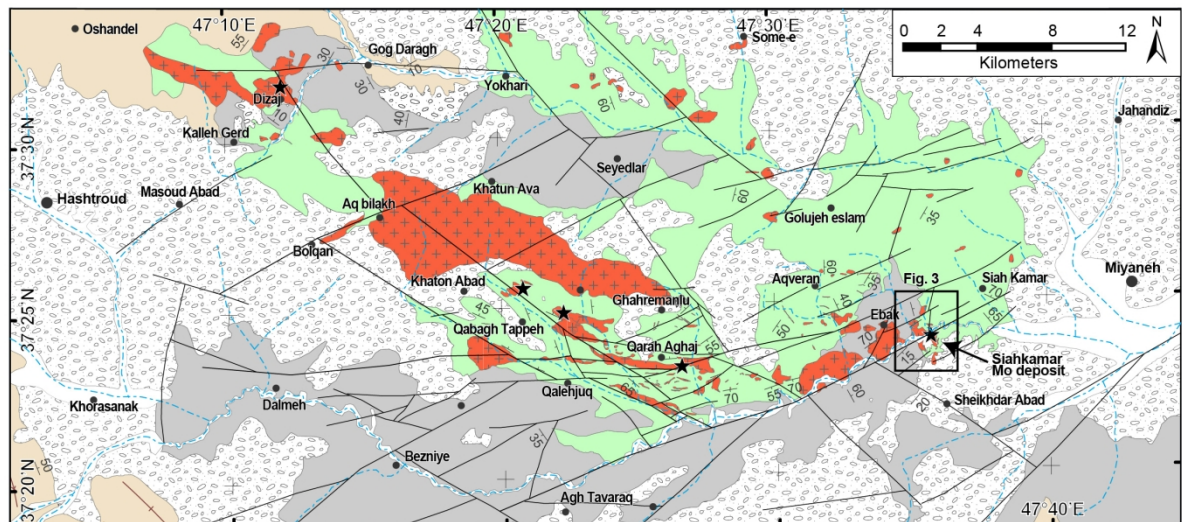
1571






1572



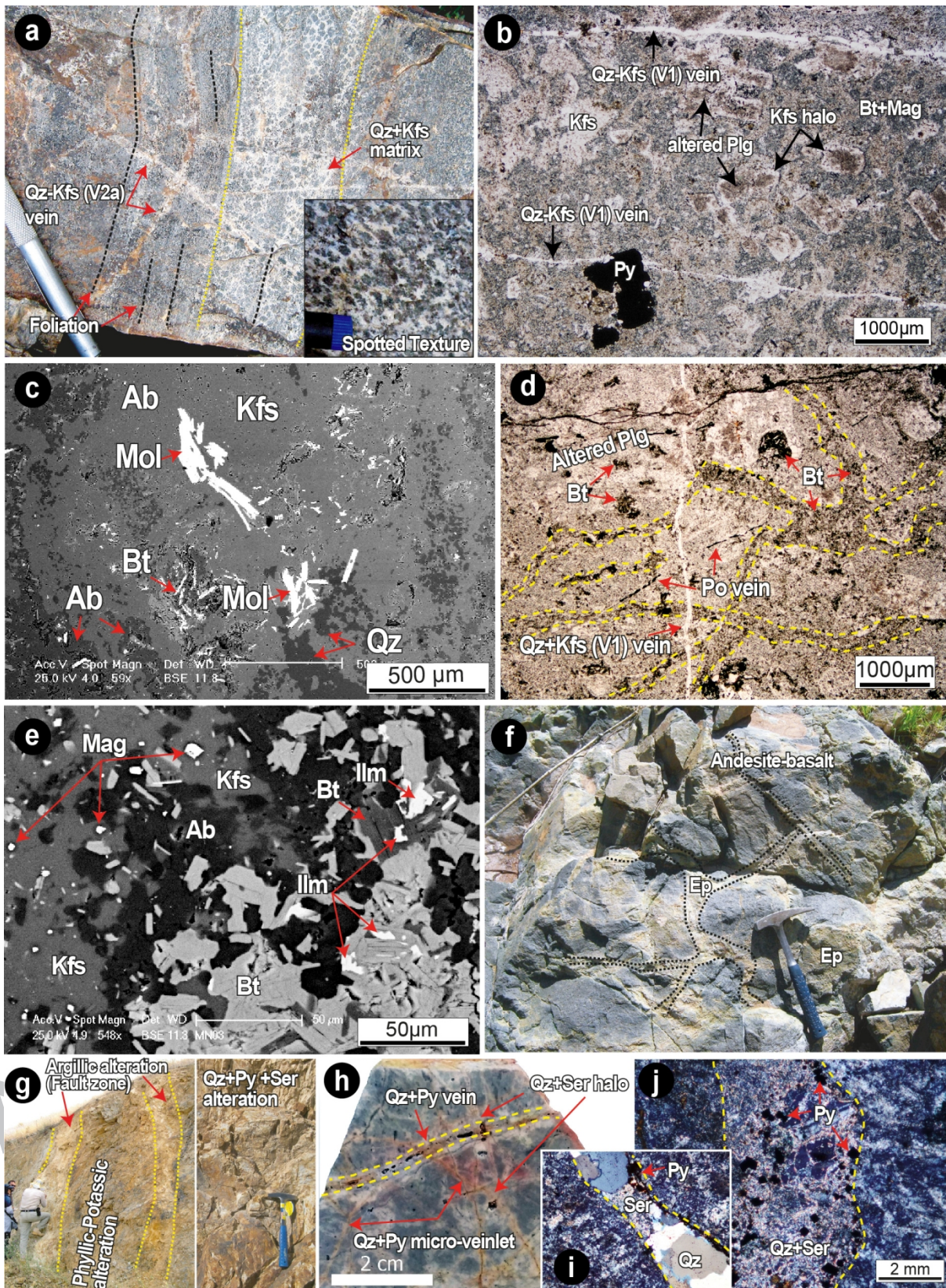
1573



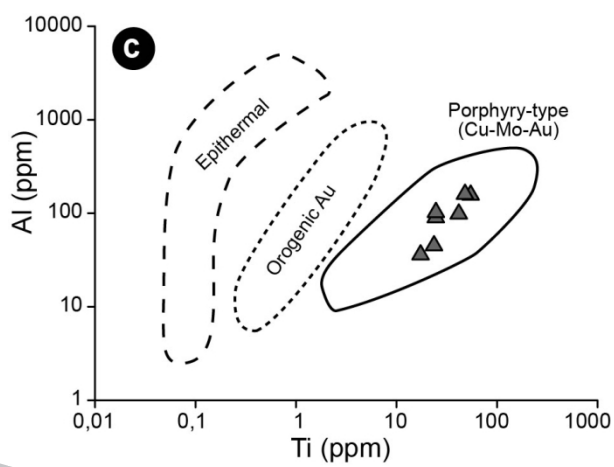
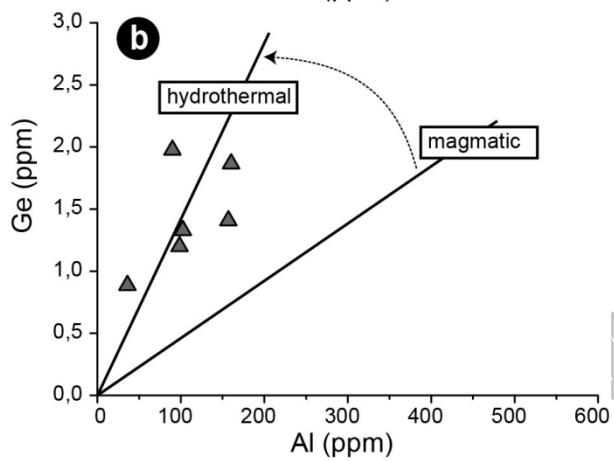
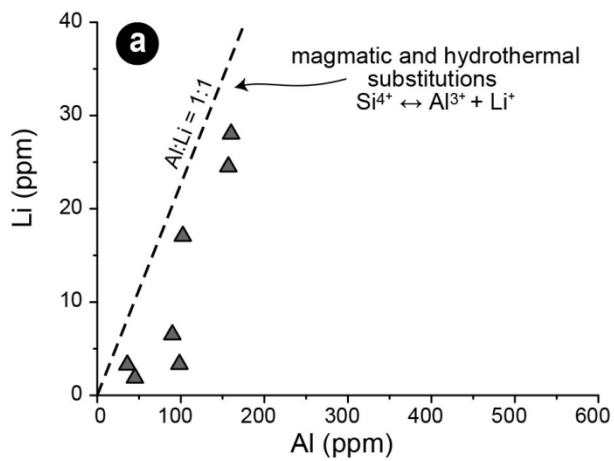
1574

Minerals	Style		Stage-1(V1)	Stage-2a (V2a)	Stage-2b (V2b)	
	Major	Minor	Na alteration	Phyllic-Silicic	Siliceous-carbonatization	Molybdenite enrichment and carbonatization
			K alteration			
Magnetite						
Albite		×				<div style="border: 1px solid black; padding: 5px;"> Mineralization styles  Disseminated  Veining  Brecciated </div>
K-Feldspar I		×				
Biotite		×				
Ilmenite						
Quartz I		×				
Pyrrhotite		×				
Molybdenite I						
Apatite		×				
K-Feldspar II	×					
Quartz II	×					
Anhydrite		×				
Scheelite		×				
Rutile		×				
Molybdenite II		×				
Pyrite		×				
Quartz III		×				
Sericite		×				
Paraspurite		×				
Ankerite	×					
Rhodochrosite	×					
Calcite	×					
Molybdenite III	×					
Hemimorphite		×				
Kaolinite		×				

1576

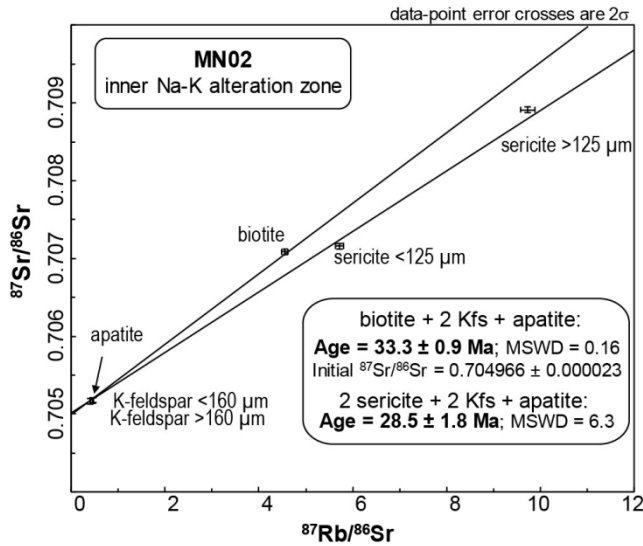


1577

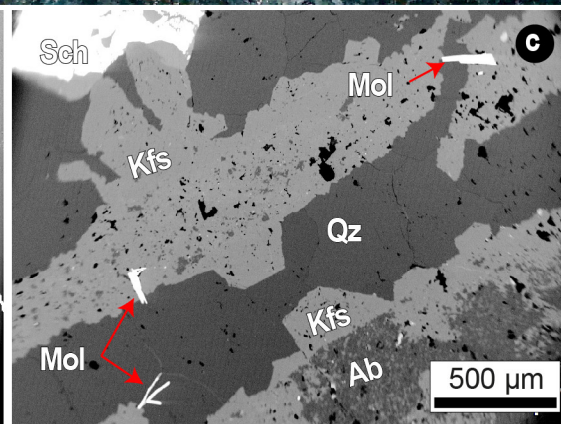
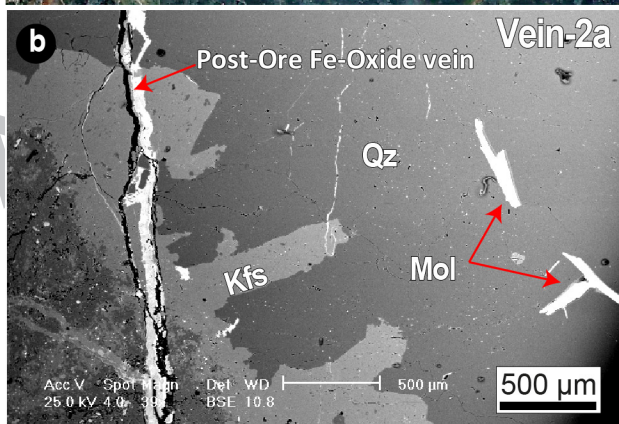
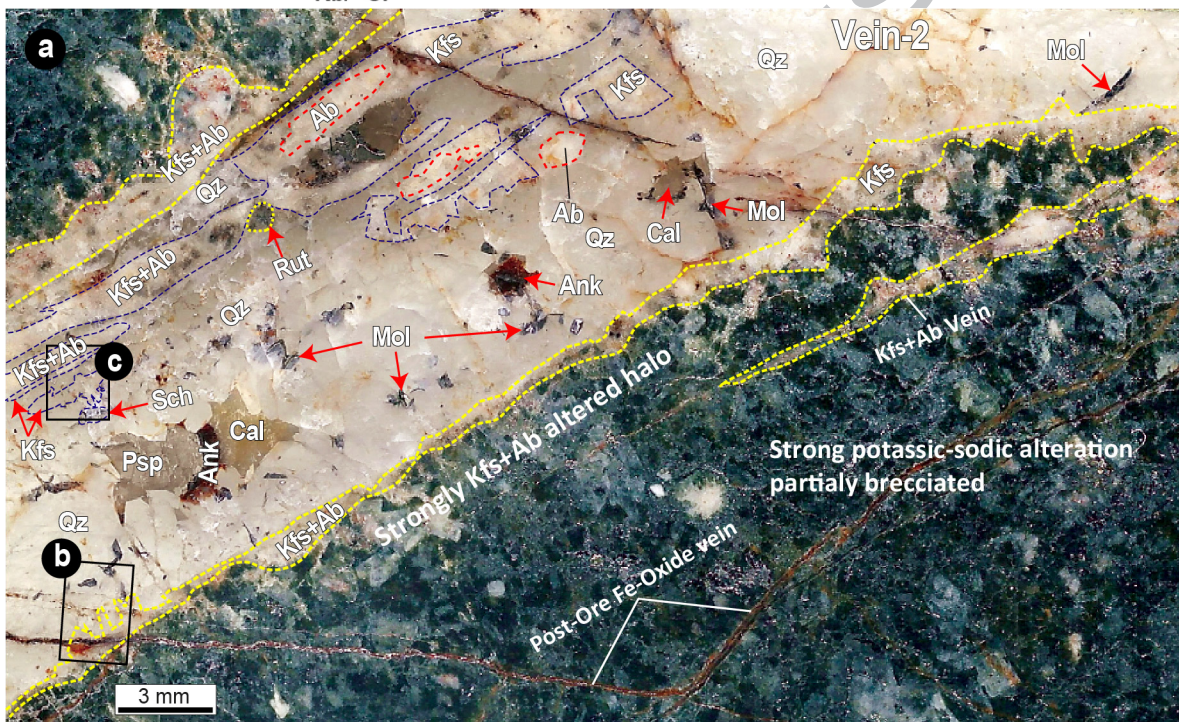


1581

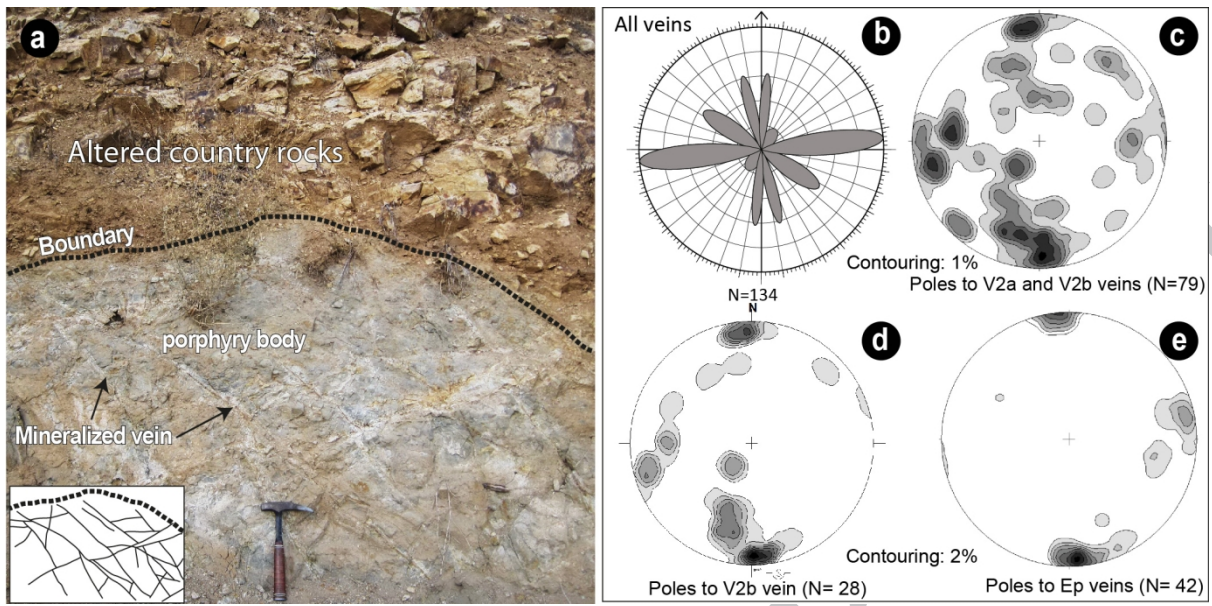
A



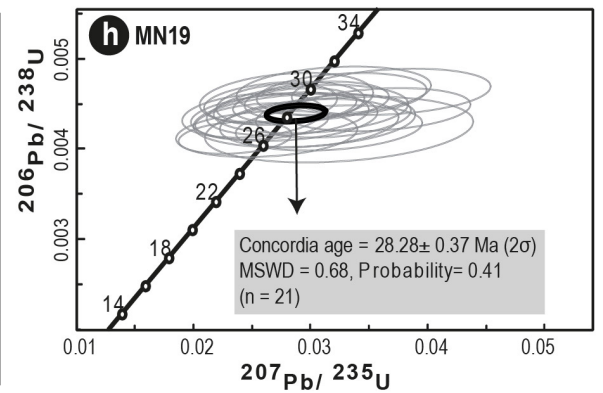
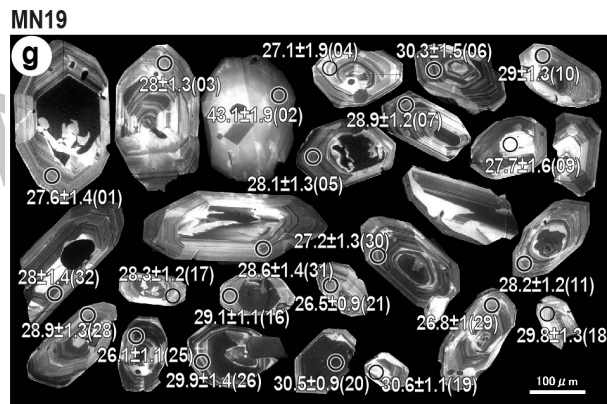
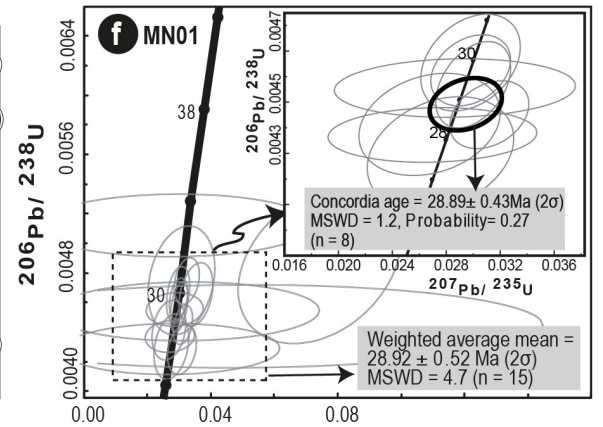
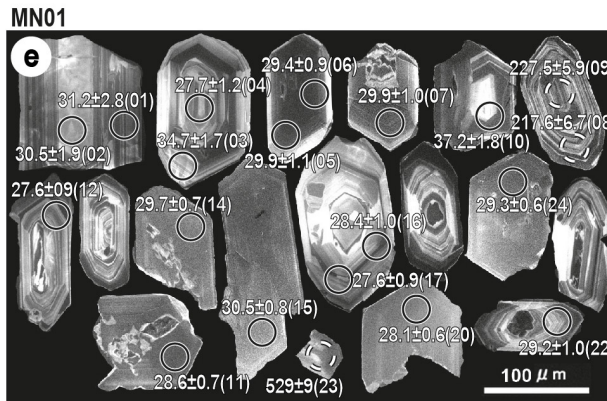
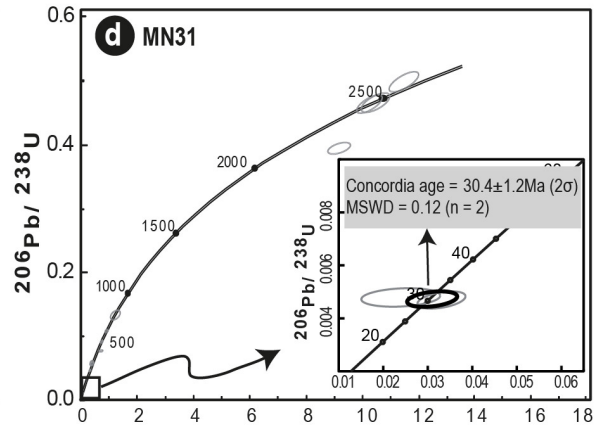
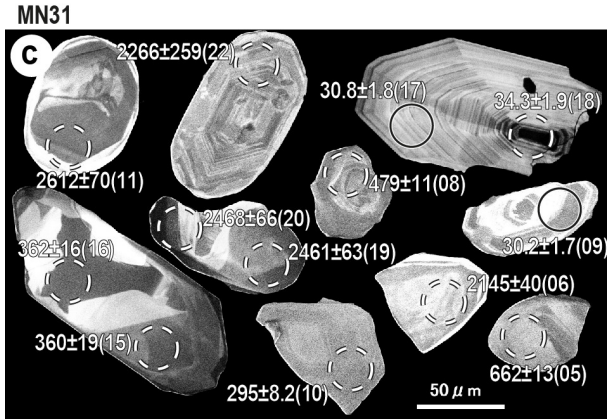
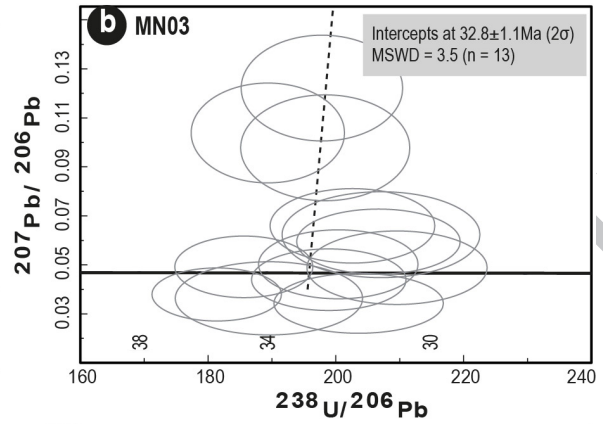
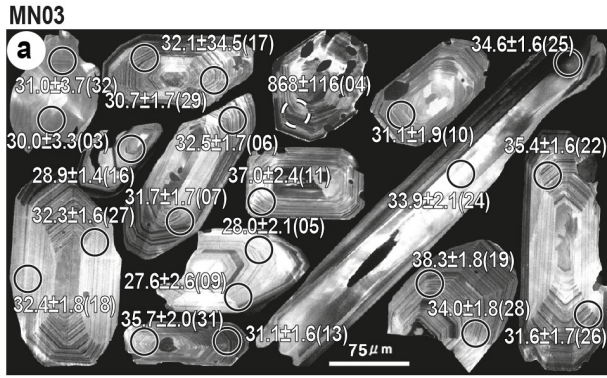
1582

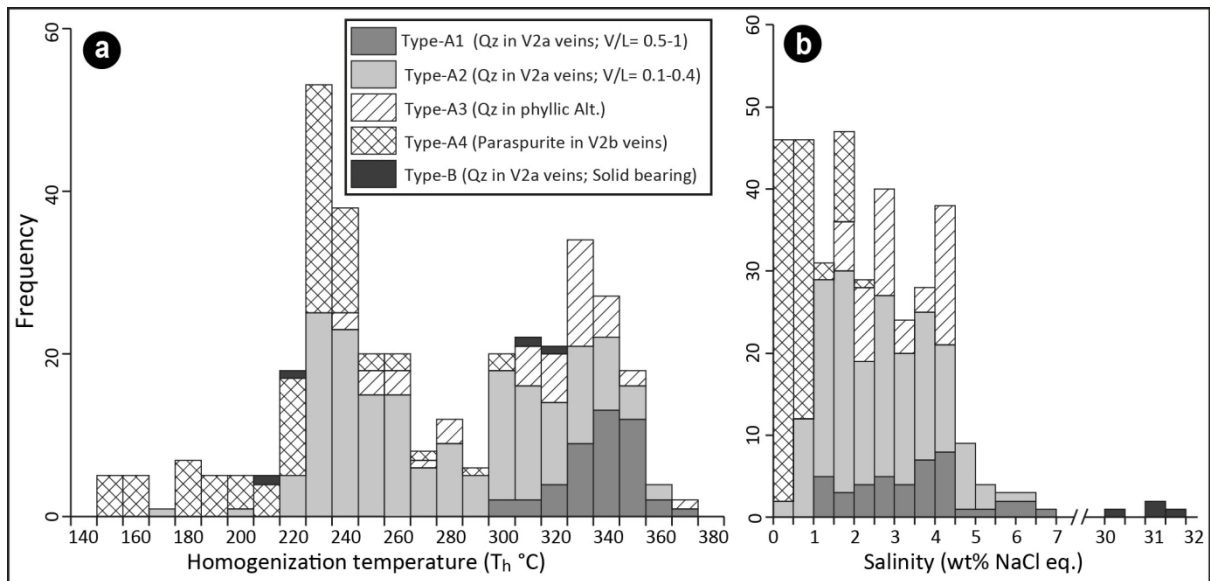


1583

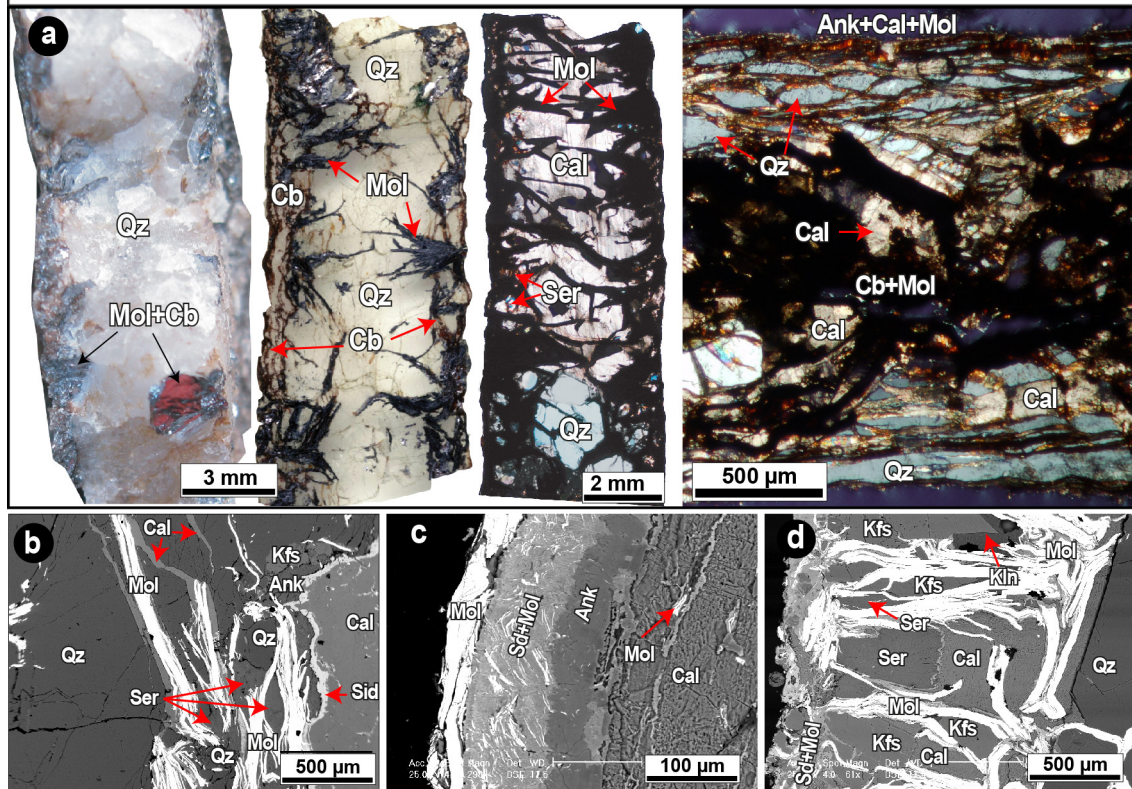


1584

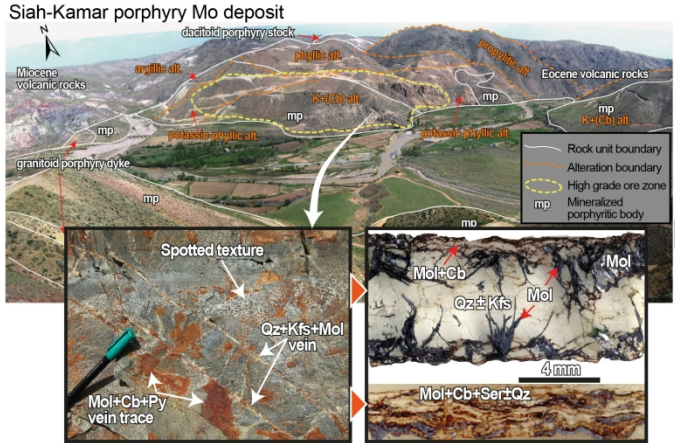
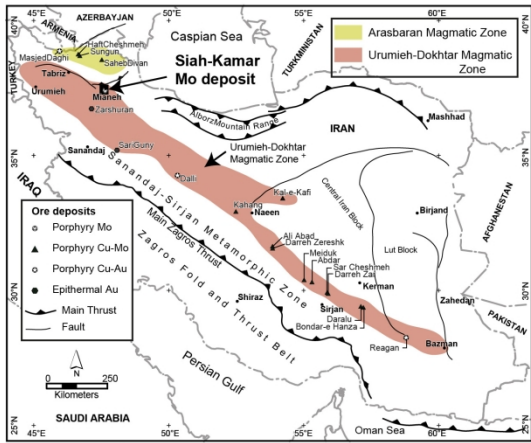




1586

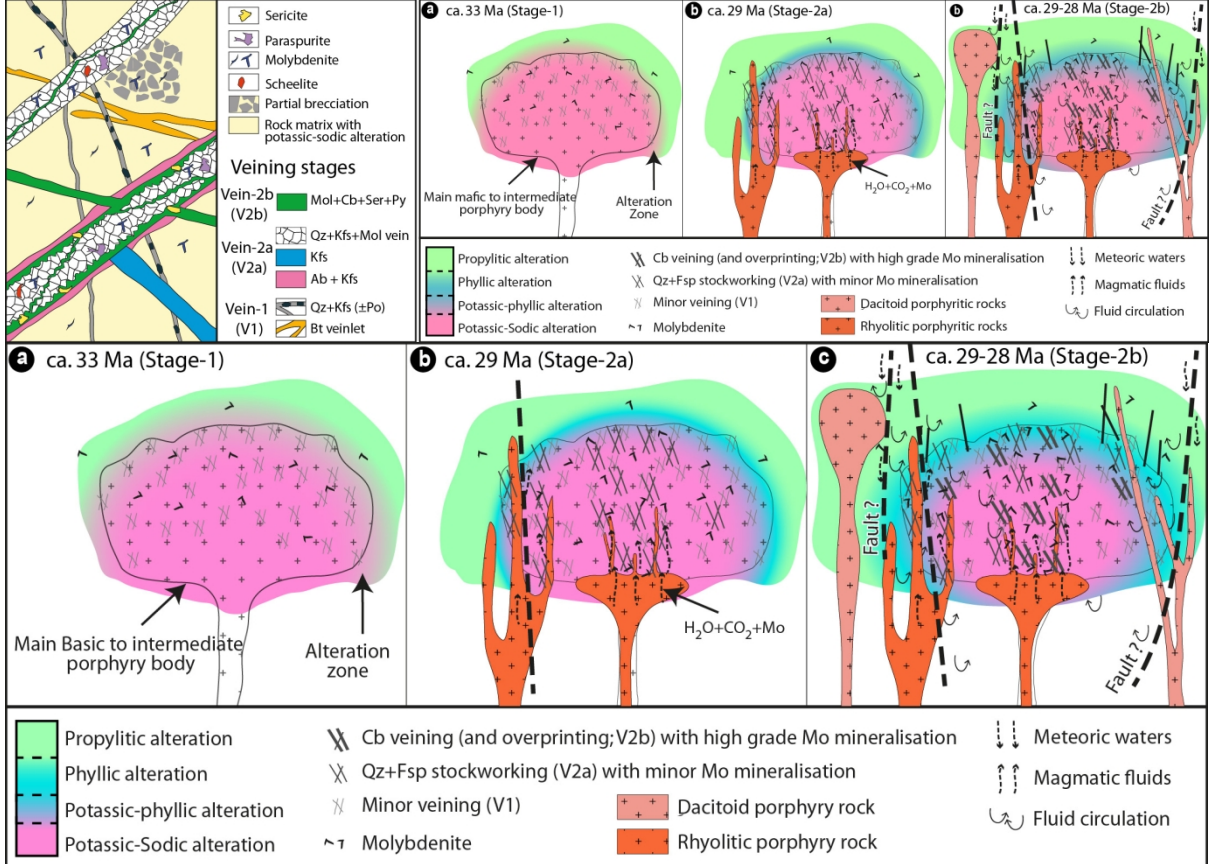


1587



Conceptual model for veining and Mo mineralisation

Model for the Siah-Kamar Mo mineralisation



1588

1589

1590

1591

1592

1593

1595

1596 **Highlights**

1597 - Long-lived magmatism and differentiation control Mo ore mineralisation

1598 - Mo ore-enhancement caused by renewed magmatism

1599 - Mo ore associated with carbonatisation, acidic fluid neutralisation and

1600 cooling

1601 - Refertilised crust leading to Mo ore formation in the Urumieh-Dokhtar zone

1602

ACCEPTED MANUSCRIPT